

LJMU Research Online

Agudo, I, Liodakis, I, Otero-Santos, J, Middei, R, Marscher, A, Jorstad, S, Zhang, H, Li, H, Di Gesu, L, Romani, RW, Kim, DE, Fenu, F, Marshall, HL, Pacciani, L, Pedrosa, JE, Aceituno, FJ, Agís-González, B, Bonnoli, G, Casanova, V, Morcuende, D, Pirola, V, Sota, A, Kouch, PM, Lindfors, E, McCall, C, Jermak, HE, Steele, IA, Borman, GA, Grishina, TS, Hagen-Thorn, VA, Kopatskaya, EN, Larionova, EG, Morozova, DA, Savchenko, SS, Shishkina, EV, Troitskiy, IS, Troitskaya, YV, Vasilyev, AA, Zhovtan, AV, Myserlis, I, Gurwell, M, Keating, G, Rao, R, Kang, S, Lee, S-S, Kim, S, Cheong, WY, Jeong, HW, Angelakis, E, Kraus, A, Blinov, D, Maharana, S, Bachev, R, Jormanainen, J, Nilsson, K, Fallah Ramazani, V, Casadio, C, Fuentes, A, Traianou, E, Thum, C, Gómez, JL, Antonelli, LA, Bachetti, M, Baldini, L, Baumgartner, WH, Bellazzini, R, Bianchi, S, Bongiorno, SD, Bonino, R, Brez, A, Bucciantini, N, Capitanio, F, Castellano, S, Cavazzuti, E, Chen, C-T, Ciprini, S, Costa, E, De Rosa, A, Del Monte, E, Di Lalla, N, Di Marco, A, Donnarumma, I, Doroshenko, V, Dovčiak, M, Ehlert, SR, Enoto, T, Evangelista, Y, Fabiani, S, Ferrazzoli, R, García, JA, Gunji, S, Hayashida, K, Heyl, J, Iwakiri, W, Kaaret, P, Karas, V, Kislat, F, Kitaguchi, T, Kolodziejczak, JJ, Krawczynski, H, La Monaca, F, Latronico, L, Maldera, S, Manfreda, A, Marin, F, Marinucci, A, Massaro, F, Matt, G, Mitsuishi, I, Mizuno, T, Muleri, F, Negro, M, Ng, C-Y, O'Dell, SL, Omodei, N, Oppedisano, C, Papitto, A, Pavlov, GG, Peirson, AL, Perri, M, Pesce-Rollins, M, Petrucci, P-O, Pilia, M, Possenti, A, Poutanen, J, Puccetti, S, Ramsey, BD, Rankin, J, Ratheesh, A, Roberts, OJ, Sgrò, C, Slane, P, Soffitta, P, Spandre, G, Swartz, DA, Tamagawa, T, Tavecchio, F, Taverna, R, Tawara, Y, Tennant, AF, Thomas, NE, Tombesi, F, Trois, A, Tsygankov, SS, Turolla, R, Vink, J, Weisskopf, MC, Wu, K, Xie, F and Zane, S

High Optical-to-X-Ray Polarization Ratio Reveals Compton Scattering in BL Lacertae's Jet

<https://researchonline.ljmu.ac.uk/id/eprint/26373/>

Article

Citation (please note it is advisable to refer to the publisher's version if you intend to cite from this work)

Agudo, I, Liodakis, I, Otero-Santos, J, Middei, R, Marscher, A, Jorstad, S, Zhang, H, Li, H, Di Gesu, L, Romani, RW, Kim, DE, Fenu, F, Marshall, HL, Pacciani, L, Pedrosa, JE, Aceituno, FJ, Agís-González, B, Bonnoli, G, Casanova. V. Morcuende. D. Pirola. V. Sota. A. Kouch. PM. Lindfors. E.

LJMU has developed **LJMU Research Online** for users to access the research output of the University more effectively. Copyright © and Moral Rights for the papers on this site are retained by the individual authors and/or other copyright owners. Users may download and/or print one copy of any article(s) in LJMU Research Online to facilitate their private study or for non-commercial research. You may not engage in further distribution of the material or use it for any profit-making activities or any commercial gain.

The version presented here may differ from the published version or from the version of the record. Please see the repository URL above for details on accessing the published version and note that access may require a subscription.

For more information please contact researchonline@ljmu.ac.uk



High Optical-to-X-Ray Polarization Ratio Reveals Compton Scattering in BL Lacertae's Jet

Iván Agudo¹, Ioannis Liodakis^{2,3}, Jorge Otero-Santos^{1,4}, Riccardo Middei^{5,6,7}, Alan Marscher⁸, Svetlana Jorstad^{8,9}, Haocheng Zhang^{10,11}, Hui Li¹², Laura Di Gesu¹³, Roger W. Romani¹⁴, Dwoon E. Kim^{15,16,17}, Francesco Fenu¹³, Herman L. Marshall¹⁸, Luigi Pacciani¹⁵, Juan Escudero Pedrosa^{1,7}, Francisco José Aceituno¹, Beatriz Agís-González^{1,3}, Giacomo Bonnoli^{1,19}, Víctor Casanova¹, Daniel Morcuende¹, Vilppu Piironen²⁰, Alfredo Sota¹, Pouya M. Kouch^{20,21}, Elina Lindfors²⁰, Callum McCall²², Helen E. Jermak²², Iain A. Steele²², George A. Borman²³, Tatiana S. Grishina⁹, Vladimir A. Hagen-Thorn⁹, Evgenia N. Kopatskaya⁹, Elena G. Larionova⁹, Daria A. Morozova⁹, Sergey S. Savchenko^{9,24}, Ekaterina V. Shishkina⁹, Ivan S. Troitskiy⁹, Yulia V. Troitskaya⁹, Andrey A. Vasilyev⁹, Alexey V. Zhovtan²³, Ioannis Myserlis^{25,26}, Mark Gurwell⁷, Garrett Keating⁷, Ramprasad Rao⁷, Sincheol Kang²⁷, Sang-Sung Lee^{27,28}, Sanghyun Kim^{27,28}, Whee Yeon Cheong^{27,28}, Hyeon-Woo Jeong^{27,28}, Emmanouil Angelakis²⁹, Alexander Kraus²⁶, Dmitry Blinov^{3,30}, Siddharth Maharana³¹, Rumen Bachev³², Jenni Jormanainen^{20,21}, Kari Nilsson²¹, Vandan Fallah Ramazani^{21,33}, Carolina Casadio^{3,30}, Antonio Fuentes¹, Efthalia Traianou¹, Clemens Thum²⁵, José L. Gómez¹, Lucio Angelo Antonelli⁶, Matteo Bachetti³⁴, Luca Baldini^{35,36}, Wayne H. Baumgartner², Ronaldo Bellazzini³⁵, Stefano Bianchi³⁷, Stephen D. Bongiorno², Raffaella Bonino^{38,39}, Alessandro Brez³⁵, Niccolò Bucciantini^{40,41,42}, Fiamma Capitanio¹⁵, Simone Castellano³⁵, Elisabetta Cavazzuti¹³, Chien-Ting Chen⁴³, Stefano Ciprini^{5,44}, Enrico Costa¹⁵, Alessandra De Rosa¹⁵, Ettore Del Monte¹⁵, Niccolò Di Lalla¹⁴, Alessandro Di Marco¹⁵, Immacolata Donnarumma¹³, Victor Doroshenko⁴⁵, Michal Dovčiak⁴⁶, Steven R. Ehlert², Teruaki Enoto⁴⁷, Yuri Evangelista¹⁵, Sergio Fabiani¹⁵, Riccardo Ferrazzoli¹⁵, Javier A. García¹¹, Shuichi Gunji⁴⁸, Kiyoshi Hayashida⁴⁹, Jeremy Heyl⁵⁰, Wataru Iwakiri⁵¹, Philip Kaaret², Vladimir Karas⁴⁶, Fabian Kislat⁵², Takao Kitaguchi⁴⁷, Jeffery J. Kolodziejczak², Henric Krawczynski⁵³, Fabio La Monaca^{15,17}, Luca Latronico³⁸, Simone Maldera³⁸, Alberto Manfreda⁵⁴, Frédéric Marin⁵⁵, Andrea Marinucci¹³, Francesco Massaro^{38,39}, Giorgio Matt³⁷, Ikuyuki Mitsuishi⁵⁶, Tsunefumi Mizuno⁵⁷, Fabio Muleri¹⁵, Michela Negro⁵⁸, Chi-Yung Ng⁵⁹, Stephen L. O'Dell², Nicola Omodei¹⁴, Chiara Oppedisano³⁸, Alessandro Papitto⁶, George G. Pavlov⁶⁰, Abel L. Peirson¹⁴, Matteo Perri^{5,6}, Melissa Pesce-Rollins³⁵, Pierre-Olivier Petrucci⁶¹, Maura Pilia³⁴, Andrea Possenti³⁴, Juri Poutanen²⁰, Simonetta Puccetti⁵, Brian D. Ramsey², John Rankin¹⁵, Ajay Ratheesh¹⁵, Oliver J. Roberts⁴³, Carmelo Sgrò³⁵, Patrick Slane⁷, Paolo Soffitta¹⁵, Gloria Spandre³⁵, Douglas A. Swartz⁴³, Toru Tamagawa⁴⁷, Fabrizio Tavecchio¹⁹, Roberto Taverna⁶², Yuzuru Tawara⁵⁶, Allyn F. Tennant², Nicholas E. Thomas², Francesco Tombesi^{17,44}, Alessio Trois³⁴, Sergey S. Tsygankov²⁰, Roberto Turolla^{62,63}, Jacco Vink⁶⁴, Martin C. Weisskopf², Kinwah Wu⁶³, Fei Xie^{15,65}, and Silvia Zane⁶³

¹ Instituto de Astrofísica de Andalucía, IAA-CSIC, Glorieta de la Astronomía s/n, E-18008 Granada, Spain; iagudo@iaa.es

² NASA Marshall Space Flight Center, Huntsville, AL 35812, USA; yannis.liodakis@gmail.com

³ Institute of Astrophysics, Foundation for Research and Technology - Hellas, Voutes, 7110, Heraklion, Greece

⁴ Istituto Nazionale di Fisica Nucleare, Sezione di Padova, 35131 Padova, Italy; jorge.oter@pd.infn.it

⁵ Space Science Data Center, Agenzia Spaziale Italiana, Via del Politecnico snc, I-00133 Roma, Italy; riccardo.middei@ssdc.asi.it

⁶ INAF Osservatorio Astronomico di Roma, Via Frascati 33, 00078 Monte Porzio Catone (RM), Italy

⁷ Center for Astrophysics | Harvard & Smithsonian, 60 Garden Street, Cambridge, MA 02138, USA

⁸ Institute for Astrophysical Research, Boston University, 725 Commonwealth Avenue, Boston, MA 02215, USA; marscher@bu.edu

⁹ Saint Petersburg State University, 7/9 Universitetskaya nab., St. Petersburg, 199034, Russia

¹⁰ University of Maryland Baltimore County, Baltimore, MD 21250, USA

¹¹ NASA Goddard Space Flight Center, Greenbelt, MD 20771, USA

¹² Theoretical Division, Los Alamos National Laboratory, Los Alamos, NM 87545, USA

¹³ ASI - Agenzia Spaziale Italiana, Via del Politecnico snc, 00133 Roma, Italy

¹⁴ Department of Physics and Kavli Institute for Particle Astrophysics and Cosmology, Stanford University, Stanford, CA 94305, USA

¹⁵ INAF, Istituto di Astrofisica e Planetologia Spaziali, Via Fosso del Cavaliere 100, 00133 Roma, Italy

¹⁶ Dipartimento di Fisica, Università degli Studi di Roma "La Sapienza", Piazzale Aldo Moro 5, 00185 Roma, Italy

¹⁷ Dipartimento di Fisica, Università degli Studi di Roma "Tor Vergata", Via della Ricerca Scientifica 1, 00133 Roma, Italy

¹⁸ MIT Kavli Institute for Astrophysics and Space Research, Massachusetts Institute of Technology, 77 Massachusetts Avenue, Cambridge, MA 02139, USA

¹⁹ INAF Osservatorio Astronomico di Brera, Via E. Bianchi 46, 23807 Merate (LC), Italy

²⁰ Department of Physics and Astronomy, Quantum, Vesilinnantie 5, FI-20014 University of Turku, Finland

²¹ Finnish Centre for Astronomy with ESO (FINCA), 20014, University of Turku, Finland

²² Astrophysics Research Institute, Liverpool John Moores University, Liverpool Science Park IC 2, 146 Brownlow Hill, UK

²³ Crimean Astrophysical Observatory RAS, P/O Nauchny, 298409, Crimea, Russia

²⁴ Pulkovo Observatory, St. Petersburg, 196140, Russia

²⁵ Institut de Radioastronomie Millimétrique, Avenida Divina Pastora, 7, Local 20, E-18012 Granada, Spain

²⁶ Max-Planck-Institut für Radioastronomie, Auf dem Hügel 69, D-53121 Bonn, Germany

²⁷ Korea Astronomy and Space Science Institute, 776 Daedeok-daeo, Yuseong-gu, Daejeon 34055, Republic of Korea

²⁸ University of Science and Technology, Korea, 217 Gajeong-ro, Yuseong-gu, Daejeon 34113, Republic of Korea

²⁹ Orchideenweg 8, 53123 Bonn, Germany

³⁰ Department of Physics, University of Crete, 70013, Heraklion, Greece

³¹ South African Astronomical Observatory, PO Box 9, Observatory, 7935, Cape Town, South Africa

³² Institute of Astronomy and NAO, Bulgarian Academy of Sciences, 1784 Sofia, Bulgaria

- ³³ Aalto University Metsähovi Radio Observatory, Metsähovintie 114, FI-02540 Kylmälä, Finland
³⁴ INAF Osservatorio Astronomico di Cagliari, Via della Scienza 5, 09047 Selargius (CA), Italy
³⁵ Istituto Nazionale di Fisica Nucleare, Sezione di Pisa, Largo B. Pontecorvo 3, 56127 Pisa, Italy
³⁶ Dipartimento di Fisica, Università di Pisa, Largo B. Pontecorvo 3, 56127 Pisa, Italy
³⁷ Dipartimento di Matematica e Fisica, Università degli Studi Roma Tre, Via della Vasca Navale 84, 00146 Roma, Italy
³⁸ Istituto Nazionale di Fisica Nucleare, Sezione di Torino, Via Pietro Giuria 1, 10125 Torino, Italy
³⁹ Dipartimento di Fisica, Università degli Studi di Torino, Via Pietro Giuria 1, 10125 Torino, Italy
⁴⁰ INAF Osservatorio Astrofisico di Arcetri, Largo Enrico Fermi 5, 50125 Firenze, Italy
⁴¹ Dipartimento di Fisica e Astronomia, Università degli Studi di Firenze, Via Sansone 1, 50019 Sesto Fiorentino (FI), Italy
⁴² Istituto Nazionale di Fisica Nucleare, Sezione di Firenze, Via Sansone 1, 50019 Sesto Fiorentino (FI), Italy
⁴³ Science and Technology Institute, Universities Space Research Association, Huntsville, AL 35805, USA
⁴⁴ Istituto Nazionale di Fisica Nucleare, Sezione di Roma “Tor Vergata”, Via della Ricerca Scientifica 1, 00133 Roma, Italy
⁴⁵ Institut für Astronomie und Astrophysik, Universität Tübingen, Sand 1, 72076 Tübingen, Germany
⁴⁶ Astronomical Institute of the Czech Academy of Sciences, Bočný II 1401/1, 14100 Praha 4, Czech Republic
⁴⁷ RIKEN Cluster for Pioneering Research, 2-1 Hirosawa, Wako, Saitama 351-0198, Japan
⁴⁸ Yamagata University, 1-4-12 Kojirakawa-machi, Yamagata-shi 990-8560, Japan
⁴⁹ Osaka University, 1-1 Yamadaoka, Suita, Osaka 563-0871, Japan
⁵⁰ University of British Columbia, Vancouver, BC V6T 1Z4, Canada
⁵¹ International Center for Hadron Astrophysics, Chiba University, Chiba 263-8522, Japan
⁵² Department of Physics and Astronomy and Space Science Center, University of New Hampshire, Durham, NH 03824, USA
⁵³ Physics Department and McDonnell Center for the Space Sciences, Washington University in St. Louis, St. Louis, MO 63130, USA
⁵⁴ Istituto Nazionale di Fisica Nucleare, Sezione di Napoli, Strada Comunale Cinthia, 80126 Napoli, Italy
⁵⁵ Université de Strasbourg, CNRS, Observatoire Astronomique de Strasbourg, UMR 7550, 67000 Strasbourg, France
⁵⁶ Graduate School of Science, Division of Particle and Astrophysical Science, Nagoya University, Furo-cho, Chikusa-ku, Nagoya, Aichi 464-8602, Japan
⁵⁷ Hiroshima Astrophysical Science Center, Hiroshima University, 1-3-1 Kagamiyama, Higashi-Hiroshima, Hiroshima 739-8526, Japan
⁵⁸ Department of Physics and Astronomy, Louisiana State University, Baton Rouge, LA 70803, USA
⁵⁹ Department of Physics, The University of Hong Kong, Pokfulam, Hong Kong, People's Republic of China
⁶⁰ Department of Astronomy and Astrophysics, Pennsylvania State University, University Park, PA 16802, USA
⁶¹ Université Grenoble Alpes, CNRS, IPAG, 38000 Grenoble, France
⁶² Dipartimento di Fisica e Astronomia, Università degli Studi di Padova, Via Marzolo 8, 35131 Padova, Italy
⁶³ Mullard Space Science Laboratory, University College London, Holmbury St Mary, Dorking, Surrey RH5 6NT, UK
⁶⁴ Anton Pannekoek Institute for Astronomy & GRAPPA, University of Amsterdam, Science Park 904, 1098 XH Amsterdam, The Netherlands
⁶⁵ Guangxi Key Laboratory for Relativistic Astrophysics, School of Physical Science and Technology, Guangxi University, Nanning 530004, People's Republic of China

Received 2025 February 18; revised 2025 March 18; accepted 2025 March 24; published 2025 May 16

Abstract

Blazars, supermassive black hole systems with highly relativistic jets aligned with the line of sight, are the most powerful long-lived emitters of electromagnetic emission in the Universe. We report here on a radio-to-gamma-ray multiwavelength campaign on the blazar BL Lacertae with unprecedented polarimetric coverage from radio to X-ray wavelengths. The observations caught an extraordinary event on 2023 November 10–18, when the degree of linear polarization of optical synchrotron radiation reached a record value of 47.5%. In stark contrast, the Imaging X-ray Polarimetry Explorer found that the X-ray (Compton scattering or hadron-induced) emission was polarized at less than 7.4% (3σ confidence level). We argue here that this observational result rules out a hadronic origin of the high-energy emission and strongly favors a leptonic (Compton scattering) origin, thereby breaking the degeneracy between hadronic and leptonic emission models for BL Lacertae and demonstrating the power of multiwavelength polarimetry to address this question. Furthermore, the multiwavelength flux and polarization variability, featuring an extremely prominent rise and decay of the optical polarization degree, is interpreted for the first time by the relaxation of a magnetic “spring” embedded in the newly injected plasma. This suggests that the plasma jet can maintain a predominant toroidal magnetic field component parsecs away from the central engine.

Unified Astronomy Thesaurus concepts: Active galaxies (17); BL Lacertae objects (158); Relativistic jets (1390); Non-thermal radiation sources (1119)

1. Introduction

The most remarkable properties of blazars, the most powerful class of active galactic nuclei, whose relativistic jets point at a small angle to the line of sight (R. Blandford et al. 2019), are produced by light-travel effects and relativistic aberration of their broadband radiation. While it is well established that the low-energy component of the spectral energy distribution (SED) of blazars is dominated by nonthermal synchrotron radiation, the nature of their high-energy emission component is a pressing

question in high-energy astrophysics. Models based on both leptonic (L. Maraschi et al. 1992; C. D. Dermer & R. Schlickeiser 1993) and hadronic (F. A. Aharonian 2000) origins of this radiation have been proposed but without solid evidence to rule out one or the other (see T. Hovatta & E. Lindfors 2019 and references therein). The latter requires the presence of highly relativistic protons accelerated in the jet. If hadronic processes were confirmed, supermassive black hole system jets would be the most plausible candidates for the origin of the recently observed extragalactic high-energy neutrinos (IceCube Collaboration et al. 2018) and ultra-high-energy cosmic rays (e.g., Telescope Array Collaboration et al. 2023). This would offer new ways for studying fundamental particle physics in extreme regimes. Simultaneous broadband polarimetry from radio wavelengths to



Original content from this work may be used under the terms of the Creative Commons Attribution 4.0 licence. Any further distribution of this work must maintain attribution to the author(s) and the title of the work, journal citation and DOI.

X-rays, which is now possible thanks to the novel capabilities of the Imaging X-ray Polarimetry Explorer (IXPE; M. C. Weisskopf et al. 2022), can finally settle this debate, as different models predict different behaviors of the low- and high-energy polarized emission (e.g., H. Zhang & M. Böttcher 2013; A. L. Peirson & R. W. Romani 2019; A. L. Peirson et al. 2022).

Blazars are prime candidates for such studies. In particular, those blazars where the emission of the low-energy component peaks at infrared frequencies, namely, low- (LSP) and intermediate-synchrotron-peaked (ISP) blazars (A. A. Abdo et al. 2010), are ideal targets for investigating the origin of the high-energy emission, as their X-ray emission arises mainly from the high-energy component. BL Lacertae (BL Lac), the archetype of the BL Lac subclass of blazars, is often classified as LSP, with $\nu_{\text{syn}} \approx 4 \times 10^{13}$ Hz (see M. Ajello et al. 2020; B. Lott et al. 2020). However, during some flaring states it becomes an ISP blazar ($\nu_{\text{syn}} > 10^{14}$ Hz). BL Lac has been the target of three previous IXPE observations (R. Middei et al. 2023; A. L. Peirson et al. 2023), two in the LSP and one in the ISP state. Thus far, polarization in the IXPE 2–8 keV band remains undetected, although during the ISP state observed in 2022 November, A. L. Peirson et al. (2023) reported significant polarization of $\sim 22\%$ in the 2–4 keV subband.

2. Results

BL Lac was observed by IXPE for approximately 500 ks during 2023 November 7–17. These observations were made during a low state of emission in the γ -ray range, although the flux in the synchrotron-dominated spectral ranges was elevated. In particular, at short millimeter wavelengths, the flux was at the highest level ever reported, while the optical and X-ray fluxes were at moderately high levels; see Figure 1.

Several ground-based and spaceborne telescopes in the radio, millimeter, optical, and X-ray bands observed BL Lac during this IXPE observation; see the Appendix, where details about the instruments, observing dates, and data reduction and analysis are provided. Using several telescopes across the world, we were able to achieve nearly uninterrupted optical polarization coverage throughout the IXPE observation. No significant X-ray polarization was detected in the 2–8 keV band, similar to the previous IXPE observations. We are able to place a 99.73% (3σ) confidence level upper limit on the polarization degree of $\Pi_X < 7.4\%$ in that band (2–8 keV); see Appendix B.3. A recent analysis of our IXPE data (A. Mondal et al. 2025) also resulted in a nondetection of the linear polarization. A. Mondal et al. (2025) gave a less constraining upper limit of $\Pi_X < 7.5\%$ at a 99% confidence level. Our $\Pi_X < 7.4\%$ upper limit therefore constitutes the most stringent constraint on the polarization degree from an LSP/ISP blazar and almost a factor of 2 improvement over previous IXPE observations of BL Lac. The presence of variability in the polarization direction would lead to incoherent averaging of the polarization vectors, partially canceling any polarization signal (e.g., L. Di Gesu et al. 2023). We tested for such variability of the X-ray polarization using four independent methodologies; see Appendix B.4. None of the tests provided high-significance ($\gg 3\sigma$) evidence of rotation of the polarization angle; see Appendix B.4.

During the IXPE observation, the measured optical polarization reached a maximum level of $\Pi_O = 47.5\% \pm 0.4\%$ (Figure 2). This is the most highly polarized state ever reported for BL Lac and rivals the maximum measured in any blazar

(e.g., P. S. Smith 2017). The short millimeter wavelength (1.3 mm, 225.5 GHz) polarization increased to $\Pi_{\text{mm}} \sim 10\%$, following a similar trend as at optical wavelengths, both in polarization degree and angle. During the optical polarization flare, we also observed total flux brightening in the millimeter, optical, and X-ray bands (see Figure 1 and the Appendix). The infrared (IR) to optical and γ -ray spectral indices (-1.39 ± 0.01 and -1.31 ± 0.08 , respectively) displayed similar values during the IXPE pointing, while the X-ray spectral index (-0.68 ± 0.01) lay between the millimeter-IR (-0.36 ± 0.08) and the IR-optical (-1.39 ± 0.01) values; see Figure 3 and Appendix E. The latter implies that the IR spectral index matches the X-ray slope over part of the IR wavelength range.

3. Discussion

The origin of the high-energy bump of the SED of blazar jets depends on the nature of the radiating particles. In the leptonic scenario, electrons (and also positrons, if any) dominate the emission via Compton scattering. For isotropic seed photons, radiation scattered by relativistic leptons in the jet is unpolarized (S. Bonometto & A. Saggion 1973). For an internal photon field (i.e., synchrotron self-Compton, SSC), if the emission is produced in a single localized region in the jet, the polarization of scattered radiation will be ~ 0.5 times that of the seed photon field (D. I. Nagirner & J. Poutanen 1993; J. Poutanen 1994; H. Krawczynski 2012), and the spectral index of the seed photon field should equal that of the scattered photon population. If there is energy stratification in the emission region or there are multiple emission regions, the polarization degree will be lowered by a factor of ~ 3 or even more (I. Liodakis et al. 2019; A. L. Peirson & R. W. Romani 2019; H. Zhang et al. 2024). It is also possible that energetic photons are produced by scattering by a beam of cold electrons in relativistic bulk motion. This would produce higher polarization in the X-ray than in the optical bands (M. C. Begelman & M. Sikora 1987). This scenario is rejected by our observations and also by previous IXPE results (R. Middei et al. 2023; A. L. Peirson et al. 2023; H. L. Marshall et al. 2024; P. M. Kouch et al. 2025).

In the hadronic scenario, protons can contribute to the high-energy radiation through (i) direct proton synchrotron radiation or (ii) a photo pair process that produces electrons and positrons (and other, short-lived, charged leptons), which in turn emit synchrotron radiation. If the process is localized in a single emission region, the X-ray polarization would be comparable to that in the optical bands (H. Zhang & M. Böttcher 2013; V. S. Paliya et al. 2018; H. Zhang et al. 2019). Even if there is energy stratification in the emission region or there are multiple emission regions, the polarization during a simultaneous multi-wavelength flare (i.e., with no pronounced cross-frequency time delays owing to radiative energy losses) is expected to be similar to the case of a single emission region (H. Zhang et al. 2024). If the contributing protons have a spatially extended distribution inside the jet, the X-ray polarization of the emission from the protons would be comparable to the millimeter polarization (H. Zhang et al. 2024). The expected polarization of the models is summarized in Table 1.

Given that protons have much longer cooling timescales than electrons, the X-ray polarization for proton emission processes should show less prominent variability than the optical polarization, which is due to relativistic electrons that lose

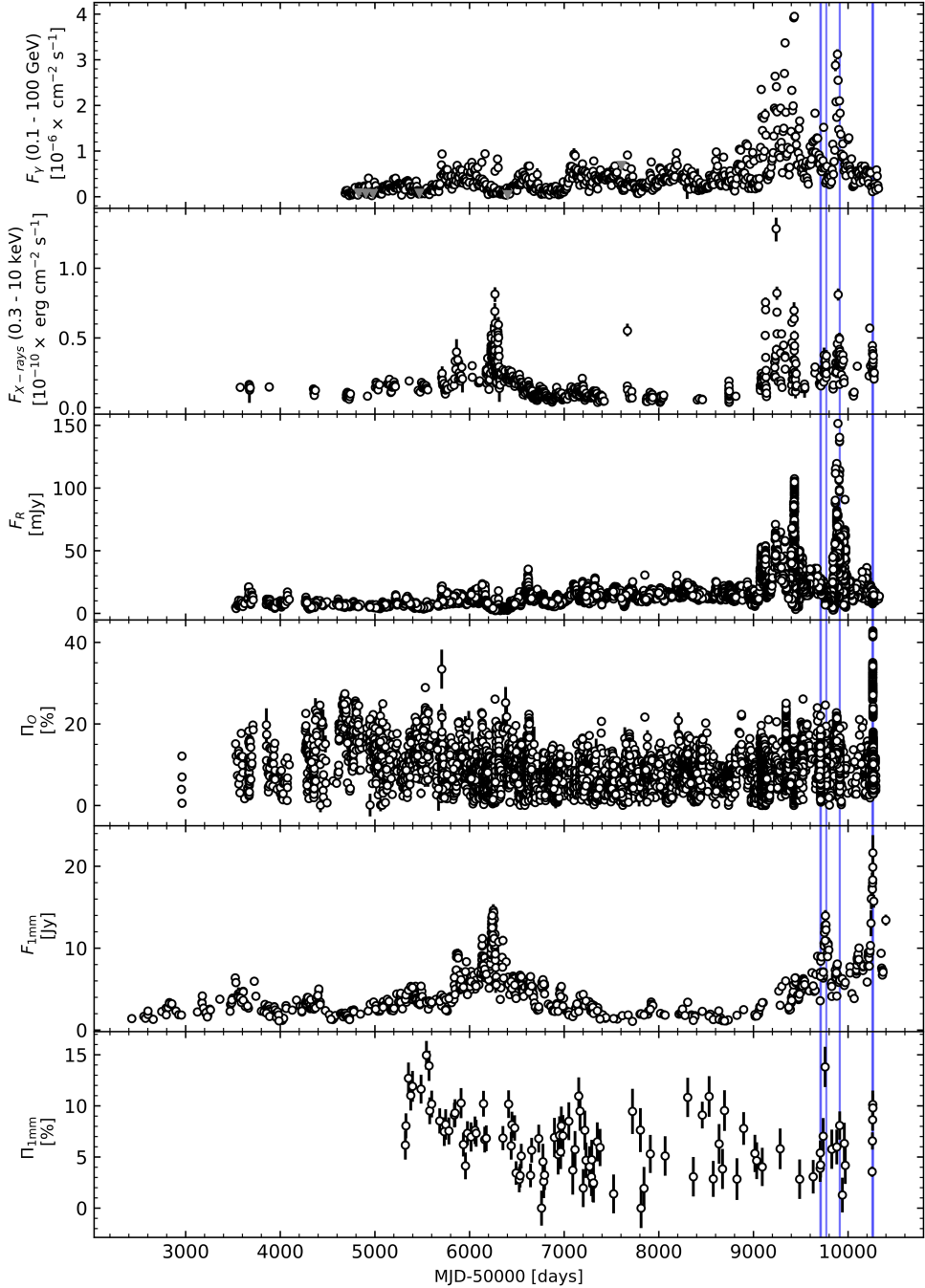


Figure 1. Historical light curves of BL Lac between 2005 and 2024. From top to bottom: γ -ray photon flux between 0.1 GeV and 100 GeV (flux points with black open markers and upper limits with gray markers), X-ray flux between 0.3 and 10 keV, optical R -band flux density, optical R -band polarization degree (%), radio 1 mm flux density, and radio 1 mm polarization degree. Blue vertical lines indicate the previous and current IXPE observations of BL Lac. A description of the origin of the data in this figure is provided in the Appendix.

energy more rapidly through emission of radiation (V. S. Paliya et al. 2018; H. Zhang et al. 2019). As we do not observe significant variability in the millimeter or optical polarization angle, no significant depolarization is expected when averaging over the duration of the IXPE observation. We find that both the millimeter and optical polarization fractions are higher than the 3σ X-ray upper limit during a significantly elevated total flux emission state at radio, optical, and X-ray bands. The optical polarization is >6 times higher than the X-ray upper limit; hence, we can reject all of the single-zone hadronic models. Based on the expectations of X-ray polarization at least

as strong as that at optical or millimeter wavelengths, the multiregion hadronic scenario can be confidently rejected as well.

The average (over the IXPE exposure) optical polarization of 25%, which is a factor of ~ 3 lower than that corresponding to a uniform magnetic field, can result from ~ 9 turbulent cells (e.g., A. P. Marscher & S. G. Jorstad 2022). In an energy-stratified shock model, the polarization should depend on frequency as $\nu^{-1/2}$ (A. P. Marscher & S. G. Jorstad 2022). The expected polarization of the energy-stratified/multizone SSC and external Compton (scattering of seed photons originating

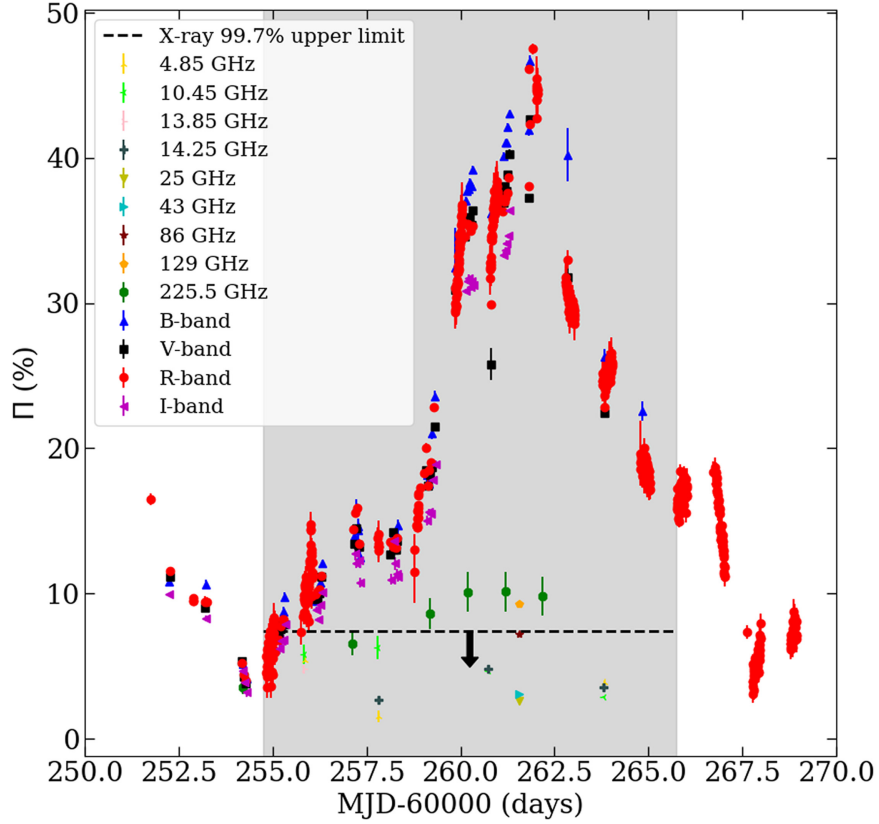


Figure 2. Multiwavelength polarization measurements during the IXPE observing campaign reported here. The gray shaded area marks the duration of the IXPE observation. The different radio and millimeter observing wavelengths and optical bands are marked with different symbols and colors, as shown in the legend. The 99.73% (3σ) upper limit of the entire integrated IXPE observation is marked with the black horizontal dashed line and arrow. The error bars correspond to the 68% (1σ) confidence interval of every measurement. MJD 60250 corresponds to 2023 November 2.

outside of the jet) emission scenarios is then between 0% and 5%. This is consistent with the IXPE upper limit. Focusing on the optical polarization peak (MJD 60261–60262.75), for an average optical polarization degree $\Pi_O = 40\%$, the SSC expectation is 14% (see H. Zhang et al. 2024). Repeating the IXPE analysis within the time interval near the peak yields a 3σ upper limit of $<21\%$, again consistent with the SSC scenario.

The optical polarization degree Π_O observed during the IXPE observation showed a dramatic increase from an initially low level, followed by a rapid decay, which provides direct evidence for a reconfiguration of global magnetic fields in the jet at ~ 1 pc from the central engine. Here we suggest a “magnetic spring” scenario as the primary mechanism accounting for this drastic variation in polarization. Before the rise in optical polarization, Π_O was $\sim 5\%$, with the polarization angle aligned along the jet direction. As jets typically possess both poloidal and toroidal magnetic components, this suggests that the toroidal magnetic field was comparable to or weaker than the poloidal and/or turbulent magnetic field components. At its peak ($\Pi_O = 47.5\% \pm 0.4\%$), the polarization angle remained aligned with the jet direction, indicating that the toroidal component became at least 2.5 times stronger than the poloidal and/or turbulent components. We suggest that this could be caused by an injection of a magnetic “spring” with a dominant toroidal configuration embedded in the jet plasma flowing outward from the central engine. Such an injection could arise from a magnetic eruption from a magnetically arrested disk (e.g., B. Ripperda et al. 2022), and it continues into the relativistic jet (H. Yang et al. 2024).

Subsequently, the rise and fall of the optical polarization over ~ 2 weeks imply a rapid relaxation of the injected toroidal component in a compact region (~ 0.1 pc) such that the toroidal component eventually becomes comparable to the poloidal components, as could occur through a kink instability in the jet (X. Guan et al. 2014; R. Barniol Duran et al. 2017). The relaxation time of the toroidal component via kink instabilities is on the order of the Alfvén crossing time, which is about 1 week for typical blazars (H. Zhang et al. 2017). The observed approximately symmetric rise and fall in Π_O suggest that magnetic fields in this jet play an active role in restoring their configurations, different from a low-magnetization plasma environment where the rise and fall in Π_O are not expected to be symmetric (H. Zhang et al. 2016). With a kink instability, some of the toroidal magnetic field can be converted into the poloidal component, reducing Π_O and contributing to the curved jet morphology observed in Very Long Baseline Array (VLBA) images (Figure 9).

The injection of a toroidally dominated magnetic spring can also account for the multiwavelength flaring behavior. This injection leads to a sudden increase of the total magnetic field strength, producing the historically high flare in the millimeter band. This flare occurs near the low-energy spectral turnover, with synchrotron radiation emitted by relatively low-energy electrons (compared to those emitting at optical and X-ray wavelengths), whose cooling times are on the order of years. The fact that the millimeter-band polarization degree does not rise as much as the optical band is consistent with the scenario that millimeter-band and lower-energy emission comes from a

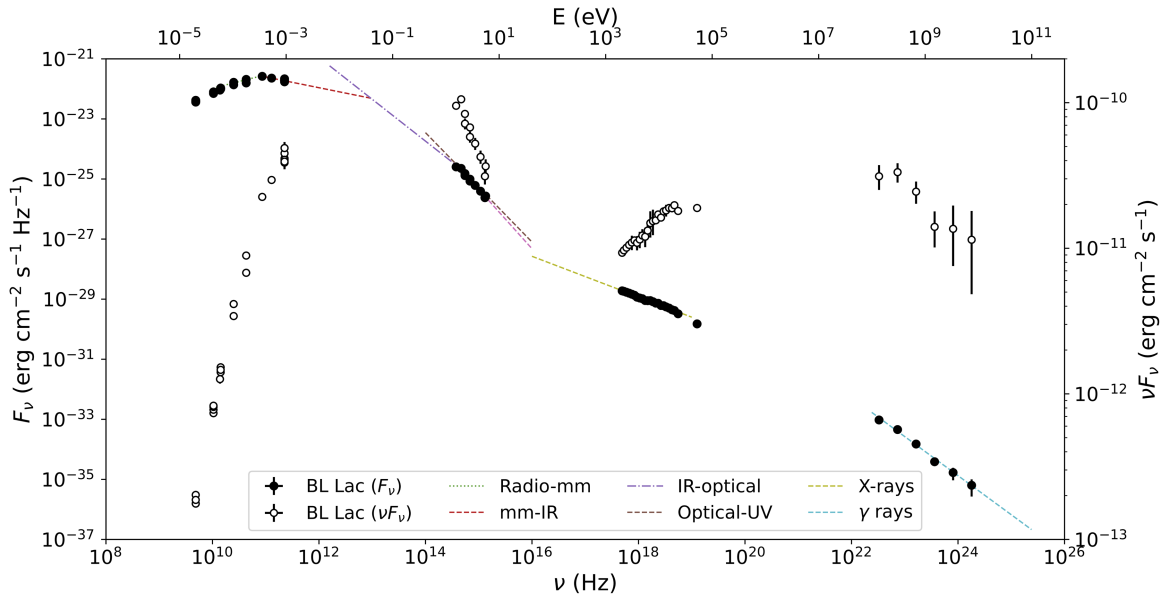


Figure 3. Flux density F_ν (black markers; in units of $\text{erg cm}^{-2} \text{s}^{-1} \text{Hz}^{-1}$) at frequency ν (Hz) and SED (open markers; in units of $\text{erg cm}^{-2} \text{s}^{-1}$) of BL Lac from radio to γ -ray frequencies during the time span of the IXPE observations. The different colored lines correspond to the power-law fits used for the estimation of the spectral indices (α , where $F_\nu \propto \nu^\alpha$) of each band, as specified in the legend and the Appendix, Table 4.

Table 1

Summary of the Multiwavelength Polarization Expectations for Different X-Ray Emission Scenarios Outlined in the Text

Model	X-Ray Polarization Degree	X-Ray Polarization Variability
Single-zone leptonic (EC)	Unpolarized	...
Single-zone leptonic (SSC)	$0.5 \times \Pi_O$	Similar to optical
Energy-stratified/multizone leptonic (SSC)	$\leq 0.3 \times \Pi_O$	Similar to millimeter
Single-zone hadronic	$\approx \Pi_O$	Less variable than optical
Energy-stratified/multizone hadronic (flare)	$\approx \Pi_O$	Less variable than optical
Energy-stratified/multizone hadronic (nonflare)	$\approx \Pi_{mm}$	Similar to millimeter

much larger volume, subject to contributions from many local magnetic field configurations and probably turbulent magnetic fields in the jet, as well as synchrotron self-absorption effects. This is consistent with the energy stratified picture reported in previous X-ray polarization observations of HSPs (A. P. Marscher & W. K. Gear 1985, I. Liodakis et al. 2022, L. Di Gesu et al. 2023, R. Middei et al. 2023, P. M. Kouch et al. 2024). This is also supported by a BL Lac analysis made by A. Mondal et al. (2025) on a similar time span using a less populated data set without optical and radio polarization information. Meanwhile, the optical band, near the high-energy turnover of the synchrotron SED, shows suppressed flaring due to enhanced synchrotron cooling (and therefore less efficient acceleration) of high-energy electrons. This is consistent with the observed softening of the optical spectral index (Table 4). Similarly, there is no prominent increase in γ -ray flux, since it is produced mainly by Compton scattering by the same electrons that emit optical synchrotron radiation.

4. Conclusion

Our results unambiguously reject single-zone hadronic processes and multizone/energy-stratified hadronic scenarios in BL

Lac. Instead, they favor a scenario where X-ray emission is dominated by Compton-scattered emission from relativistic electrons in a region with gradients in the maximum electron energy. This could be realized where electrons are accelerated in a fresh plasma blob threaded by a magnetic spring dominated by a strong toroidal magnetic field in the parsec-scale region, beyond which electrons are subsequently advected downstream. While protons may occasionally play an important role in the emission from blazar jets, and their interactions in jets might be associated with neutrino detections, our polarization study implies that this is not the typical case. Our observations constitute the strongest test of X-ray emission processes in astrophysical jets so far and the strongest evidence against relativistic protons dominating the X-ray emission in blazars. Our study also demonstrates the rich potential of multiwavelength total flux and polarimetric monitoring campaigns that include X-ray polarimetry and ultrahigh angular resolution very long baseline interferometry (VLBI) observations to resolve the long-standing question of the role that relativistic protons play in blazar jets.

Acknowledgments

The Imaging X-ray Polarimetry Explorer (IXPE) is a joint US and Italian mission. The US contribution is supported by the National Aeronautics and Space Administration (NASA) and led and managed by its Marshall Space Flight Center (MSFC), with industry partner Ball Aerospace (contract NNM15AA18C), now BAE Systems. The Italian contribution is supported by the Italian Space Agency (Agenzia Spaziale Italiana, ASI) through contract ASI-OHBI-2022-13-I.0, agreements ASI-INAF-2022-19-HH.0 and ASI-INFN-2017.13-H0, and its Space Science Data Center (SSDC) with agreements ASI-INAF-2022-14-HH.0 and ASI-INFN 2021-43-HH.0 and by the Istituto Nazionale di Astrofisica (INAF) and the Istituto Nazionale di Fisica Nucleare (INFN) in Italy. This research used data products provided by the IXPE Team (MSFC, SSDC, INAF, and INFN) and distributed with additional software tools by the High-Energy Astrophysics Science Archive Research Center (HEASARC) at NASA Goddard Space Flight Center (GSFC). Based on

observations obtained with XMM-Newton, an ESA science mission with instruments and contributions directly funded by ESA Member States and NASA. We acknowledge the use of public data from the Swift data archive. Some of the data are based on observations collected at the Observatorio de Sierra Nevada, which is owned and operated by the Instituto de Astrofísica de Andalucía (IAA-CSIC), and at the Centro Astronómico Hispano en Andalucía (CAHA), which is operated jointly by Junta de Andalucía and Consejo Superior de Investigaciones Científicas (IAA-CSIC). The Perkins Telescope Observatory, located in Flagstaff, Arizona, USA, is owned and operated by Boston University. Data from the Steward Observatory spectropolarimetric monitoring project were used. This program is supported by Fermi Guest Investigator grants NNX08AW56G, NNX09AU10G, NNX12AO93G, and NNX15AU81G. This research was partially supported by the Bulgarian National Science Fund of the Ministry of Education and Science under grants KP-06-H38/4 (2019) and KP-06-PN-68/1(2022). The Liverpool Telescope is operated on the island of La Palma by Liverpool John Moores University in the Spanish Observatorio del Roque de los Muchachos of the Instituto de Astrofísica de Canarias with financial support from the UKRI Science and Technology Facilities Council (STFC) (ST/T00147X/1). This research has made use of data from the RoboPol program, a collaboration between Caltech, the University of Crete, IA-FORTH, IUCAA, the MPIfR, and the Nicolaus Copernicus University, which was conducted at Skinakas Observatory in Crete, Greece. The data in this study include observations made with the Nordic Optical Telescope, owned in collaboration by the University of Turku and Aarhus University and operated jointly by Aarhus University, the University of Turku, and the University of Oslo, representing Denmark, Finland, and Norway; the University of Iceland; and Stockholm University at the Observatorio del Roque de los Muchachos, La Palma, Spain, of the Instituto de Astrofísica de Canarias. The data presented here were obtained in part with ALFOSC, which is provided by the Instituto de Astrofísica de Andalucía (IAA) under a joint agreement with the University of Copenhagen and NOT. The Submillimeter Array (SMA) is a joint project between the Smithsonian Astrophysical Observatory and the Academia Sinica Institute of Astronomy and Astrophysics and is funded by the Smithsonian Institution and the Academia Sinica. Maunakea, the location of the SMA, is a culturally important site for the indigenous Hawaiian people; we are privileged to study the cosmos from its summit. The POLAMI observations reported here were carried out at the IRAM 30 m telescope. IRAM is supported by INSU/CNRS (France), MPG (Germany), and IGN (Spain). The KVN is a facility operated by the Korea Astronomy and Space Science Institute. The KVN operations are supported by the Korea Research Environment Open NETwork (KREONET), which is managed and operated by the Korea Institute of Science and Technology Information (KISTI). Partly based on observations with the 100 m telescope of the Max-Planck-Institut für Radioastronomie (MPIfR) at Effelsberg. Observations with the 100 m radio telescope at Effelsberg have received funding from the European Union's Horizon 2020 research and innovation program under grant agreement No. 101004719 (ORP). The IAA-CSIC coauthors acknowledge financial support from the Spanish “Ministerio de Ciencia e Innovación” (MCIN/AEI/10.13039/501100011033) through the Center of Excellence Severo Ochoa award for the Instituto de Astrofísica de

Andalucía-CSIC (CEX2021-001131-S) and through grants PID2019-107847RB-C44 and PID2022-139117NB-C44. I.L. was supported by the NASA Postdoctoral Program at the Marshall Space Flight Center, administered by Oak Ridge Associated Universities under contract with NASA. B.A.-G. and I.L. were funded by the European Union ERC-2022-STG - BOOTES - 101076343. Views and opinions expressed are, however, those of the author(s) only and do not necessarily reflect those of the European Union or the European Research Council Executive Agency. Neither the European Union nor the granting authority can be held responsible for them. J.O.-S. acknowledges financial support from the project ref. AST22_00001_9 with funding from the European Union - NextGenerationEU, the Ministerio de Ciencia, Innovación y Universidades, Plan de Recuperación, Transformación y Resiliencia, the Consejería de Universidad, Investigación e Innovación from the Junta de Andalucía, and the Consejo Superior de Investigaciones Científicas, as well as from INFN Cap. U.1.01.01.009. This work has been partially supported by the ASI-INAF program I/004/11/4. The research at Boston University was supported in part by National Science Foundation grant AST-2108622, NASA Fermi Guest Investigator grants 80NSSC23K1507 and 80NSSC23K1508, NASA NuSTAR Guest Investigator grant 80NSSC24K0547, and NASA Swift Guest Investigator grant 80NSSC23K1145. This work was supported by NSF grant AST-2109127. H.Z. is supported by NASA under award number 80GSFC21M0002. H.Z.’s work is supported by Fermi GI program cycle 16 under award number 22-FERMI22-0015 and IXPE GO program cycle 1 under award numbers 80NSSC24K1160 and 80NSSC24K1173. Research by H.L. was supported by the Laboratory Directed Research and Development program of Los Alamos National Laboratory under project number 20220087DR. E.L. was supported by Academy of Finland projects 317636 and 320045. We acknowledge funding to support our NOT observations from the Finnish Centre for Astronomy with ESO (FINCA), University of Turku, Finland (Academy of Finland grant number 306531). S.K., S.-S.L., W.Y.C., S.-H.K., and H.-W.J. were supported by the National Research Foundation of Korea (NRF) grant funded by the Korea government (MIST) (2020R1A2C2009003). C.C. acknowledges support by the European Research Council (ERC) under the HORIZON ERC grants 2021 program under grant agreement No. 101040021. This work was supported by JST, the establishment of university fellowships toward the creation of science technology innovation, grant No. JPMJFS2129. D.B. acknowledges support from the European Research Council (ERC) under the European Union’s Horizon 2020 research and innovation program under grant agreement No. 771282.

Facility: IXPE, Swift (XRT and UVOT), XMM-Newton, NuSTAR, Fermi, Belogradchik Observatory, Calar Alto Observatory, Nordic Optical Telescope, Liverpool Telescope, LX-200, Perkins Telescope, Sierra Nevada Observatory, Skinakas Observatory, SMA, IRAM 30 m telescope, KVN, Effelsberg 100 m telescope, VLBA.

Software: HEASoft (Nasa High Energy Astrophysics Science Archive Research Center Heasarc 2014), FTOOLS (J. K. Blackburn 1995), IOP4 (J. Escudero Pedrosa et al. 2024a, 2024b), AIPS,⁶⁶ DIFMAP (M. C. Shepherd 1997), GILDAS.⁶⁷

⁶⁶ <http://www.aips.nrao.edu/aipsdoc.html>

⁶⁷ <https://www.iram.fr/IRAMFR/GILDAS/>

Appendix

The IXPE observation of BL Lac presented here was accompanied by contemporaneous observations from several ground- and space-based facilities. We give a short description of each of those facilities below. More details of the observations and data reduction, including information on the individual telescopes, can be found in L. Di Gesu et al. (2022), I. Liodakis et al. (2022), R. Middei et al. (2023), A. L. Peirson et al. (2023), and P. M. Kouch et al. (2024).

Appendix A Fermi-LAT γ -Ray Data

Data from the pair-conversion Large Area Telescope (LAT) on board the Fermi satellite are included in this work. This telescope monitors the γ -ray sky every 3 hr in the energy range of 20 MeV to \sim 2 TeV, with sensitivity highest in the 0.1–200 GeV range (W. B. Atwood et al. 2009). We have retrieved the publicly available BL Lac light curve from the Fermi-LAT public Light Curve Repository (LCR⁶⁸, see S. Abdollahi et al. 2023). This database contains the light curves of all variable sources in the 4FGL-DR2 catalog (S. Abdollahi et al. 2020; J. Ballet et al. 2020), which includes sources with a variability index >21.6 (see Table 12 in S. Abdollahi et al. 2020). We refer the reader to S. Abdollahi et al. (2023) for a detailed discussion on the automatic unbinned likelihood analysis adopted by the LCR for computing the light curves. Here, we have used the 3 day binned light curve with a freely varying spectral slope in each bin. Figure 1 shows the γ -ray light curve compiled since the beginning of operations of Fermi. The light curve shows that the γ -ray flux level of the source during the IXPE observation reported here was low to moderate.

We have derived the γ -ray portion of the SED and spectrum of BL Lac during the IXPE observation by retrieving and analyzing the data from the LAT Data Server,⁶⁹ plus an extra ± 15 days around it, i.e., between 2023 October 23 and 2023 December 3. This extended time window was selected owing to the relatively faint and stable γ -ray emission of the source in the period that is strictly simultaneous with IXPE observations, which would lead only to upper limits over that period. We have selected and analyzed all of the Pass8 P8R3_source events between 100 MeV and 300 GeV with version 1.2.23 of the standard software FERMITOOLS. A cut of 90° in zenith angle was applied to minimize the contamination from the limb of the Earth. The recommended Galactic diffuse emission model and isotropic component for the event selection and analysis performed here were employed.⁷⁰

In order to obtain a model describing all of the relevant sources in the field, a binned likelihood analysis was performed on 1 yr of LAT data (2019 January–2020 January). We included all sources contained in the defined region of interest (ROI) near BL Lac, plus those located within an additional annular region of 10° radius. For inclusion into the final model, the spectral parameters and flux normalization of all sources within the ROI were left as free parameters. For the sources within the annular region, these parameters were fixed to those from the 4FGL-DR2 catalog. The normalizations of the diffuse

components were also left as free parameters. In the convergence iteration, all sources with a test statistic of <4 (approximately 2σ significance) were removed from the final model.

Finally, we have also extracted the γ -ray spectrum and SED of BL Lac in the aforementioned time window. We used a binned likelihood analysis to model each bin of the SED with a power-law spectral model. The LAT catalogs show a significant preference for a log-parabolic spectral shape after averaging more than 14 yr of data. However, due to the short interval considered here, we do not accumulate enough statistics to observe a preference for a curved spectrum over the simpler power-law model. Hence, we adopted the latter for the SED estimated here, obtaining a power-law spectrum with an index $\alpha = -2.31 \pm 0.08$.

Appendix B X-Ray Data

B.1. IXPE Observation and Data Reduction

BL Lac was observed by IXPE’s three detector units (DUs) from 2023 November 07 00:44:08 to 2023 November 17 19:48:05 for a total exposure time of \sim 515 ks, see Table 2. The I , Q , and U spectra for each of the three DUs of IXPE were computed using the software IXPEOBSSIM (v. 31.0.1; M. Pesce-Rollins et al. 2019; L. Baldini et al. 2022) and adopting the background rejection prescriptions by A. Di Marco et al. (2023). The spectra were computed to enable the use of the weighted analysis method (A. Di Marco et al. 2022). The Stokes I , Q , and U spectra were extracted using a circular region with radius = 0.95 centered on BL Lac. The background was derived using an annular region with $r_{\text{in}(\text{out})} = 1.2(3.5)$. These choices have been shown to enhance the sensitivity to polarization, as discussed by A. Di Marco et al. (2023). The resulting I Stokes spectra were rebinned, requiring each energy bin to have a signal-to-noise ratio greater than 7. A uniform binning of 280 eV was then adopted for the Q and U Stokes spectra.

B.2. Swift, XMM-Newton, and NuSTAR Observations and Data Reduction

The IXPE observation of BL Lac was coordinated with different X-ray observatories: XMM-Newton (F. Jansen et al. 2001), the Neil Gehrels Swift Observatory (Swift; N. Gehrels et al. 2004), and the Nuclear Spectroscopic Telescope Array (NuSTAR; F. A. Harrison et al. 2013), see Table 2. This joint effort allowed us to monitor the source variability and derive the intrinsic spectral shape of the source below and above the IXPE 2–8 keV bandpass.

The X-Ray Telescope (XRT) on Swift operates in the 0.2–10 keV energy band and has a high spatial resolution of 18''. Both the XRT and UltraViolet and Optical Telescope (UVOT) operate simultaneously to enable concurrent observations in different electromagnetic bands (D. N. Burrows et al. 2005;

Table 2
Log of X-Ray Observations Related to the IXPE Pointings of BL Lac

Observatory	Obs. ID	Obs. Date (yyyy/mm/dd)	Net Exp. (ks)
IXPE	02009701	2023/11/07–17	\sim 515
NuSTAR	80901639002	2023/11/13–14	\sim 20
XMM-Newton	0902112601	2023/11/17	\sim 5

⁶⁸ <https://fermi.gsfc.nasa.gov/ssc/data/access/lat/LightCurveRepository/about.html>

⁶⁹ <https://fermi.gsfc.nasa.gov/ssc/data/access/lat/>

⁷⁰ <https://fermi.gsfc.nasa.gov/ssc/data/access/lat/BackgroundModels.html>

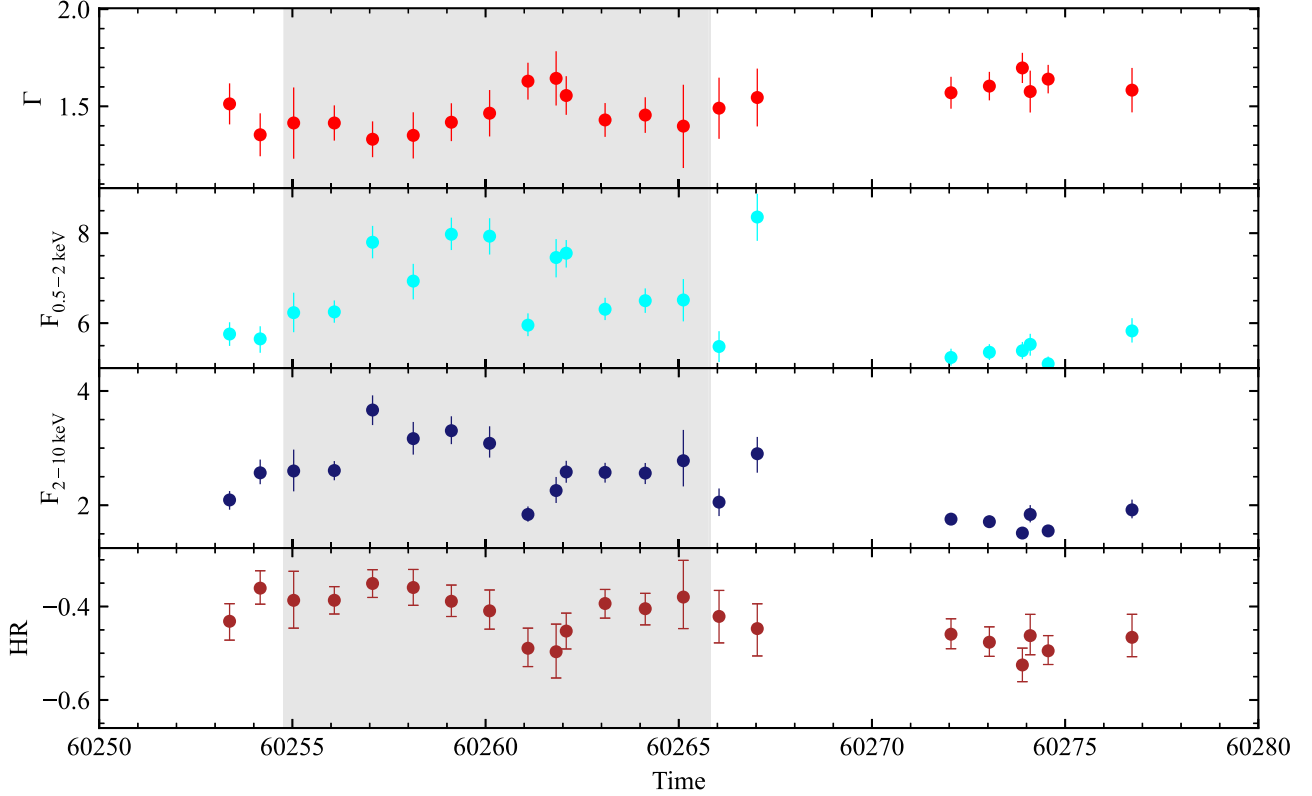


Figure 4. Results of the Swift-XRT monitoring campaign of BL Lac. Fluxes $F_{0.5-2 \text{ keV}}$ and $F_{2-10 \text{ keV}}$ are displayed in units of $10^{-12} \text{ erg cm}^{-2} \text{ s}^{-1}$ and $10^{-11} \text{ erg cm}^{-2} \text{ s}^{-1}$, respectively. The label “HR” stands for hardness ratio, which we define as $(F_{2-10 \text{ keV}} - F_{0.5-2 \text{ keV}})/(F_{2-10 \text{ keV}} + F_{0.5-2 \text{ keV}})$. Gray shaded areas mark the duration of the IXPE pointing.

P. W. A. Roming et al. 2005). We retrieved the reduced X-ray, UV, and optical data from the Swift public mirror archive⁷¹ of the Space Science Data Center (SSDC) at the Italian Space Agency (ASI). Swift-XRT observed BL Lac in photon-counting readout mode. The data were first reprocessed locally with the XRTDAS software package (version family v3.7.0), developed by the ASI-SSDC and included in the NASA-HEASARC HEAsoft package⁷² (version family v6.31.1). Standard calibration and filtering processing steps were adopted, and the calibration files available from the Swift-XRT CALDB (version family 20220803) were used. The science products were extracted using a circle of 20 pixels ($47''$) radius centered on the target source, while the background was derived from a nearby circular region with a radius of 40 pixels. All the spectra were subsequently binned with the family grppha tool of the FTOOLS package⁷³ requiring each bin to have a minimum of five counts and then modeled using the XSPEC software package⁷⁴ while adopting a single power-law model with foreground photoelectric absorption from gas in our Galaxy. In Figure 4, we show the temporal behavior of the power-law slope (photon index), soft and hard fluxes (0.5–2 and 2–10 keV, respectively), and hardness ratios of BL Lac. The UVOT on board Swift is capable of observations in the [170, 600] nm band performed simultaneously with Swift-XRT. In our case, the UVOT pointed at BL Lac with filters V 5468 Å, B 4392 Å, U 3465 Å, UVW1 2600 Å, UVM2 2246 Å,

and UVW2 1928 Å. We derived the photometric points for each filter for the different observations using the standard tools within an automated reduction procedure. We adopted two regions, including a circular one centered on the source (radius = $2''$) for estimating the counts from the target, while a concentric annulus ($\Delta\text{radius} = 7''$), free of any other sources or spurious detection, was used to determine the background. We show the returned count rates for the UVOT filters, uncorrected for Galactic or intrinsic reddening, in Figure 4.

XMM-Newton, which is sensitive to soft X-rays, briefly observed BL Lac for about 5 ks, from 2023 November 17 12:21:37 to 2023 November 17 19:08:46. The satellite’s EPIC-pn camera (L. Strüder et al. 2001) observed BL Lac in small window mode, with the medium filter applied. Data were processed with the standard XMM-Newton Science Analysis System (SAS v21; C. Gabriel et al. 2004). Source extraction radii and screening for high-background intervals were determined through an iterative process (E. Piconcelli et al. 2004) that maximizes the signal-to-noise ratio. The background was extracted from circular regions with a radius of $50''$, and the same shape centered on BL Lac was adopted for science products. The resulting third-level products were grouped by requiring each bin to contain at least 30 counts and not to oversample the spectral resolution by a factor larger than 3. The net count rate was less than the maximum allowed limit of 50 counts s^{-1} to avoid a deteriorated response due to photon pileup for EPIC-pn observations in small window mode (e.g., P. Jethwa et al. 2015). We further assessed the potential impact of pileup in the XMM-Newton observation by means of the epatplot task, a standard SAS command devoted to checking for any pileup affecting the data, and we found it to be negligible.

⁷¹ Available at <https://swift.sscdc.asi.it/>.

⁷² Available at <https://heasarc.gsfc.nasa.gov/docs/software/heasoft/>.

⁷³ Available at <https://heasarc.gsfc.nasa.gov/ftools/>.

⁷⁴ Available at <https://heasarc.gsfc.nasa.gov/xanadu/xspec/>.

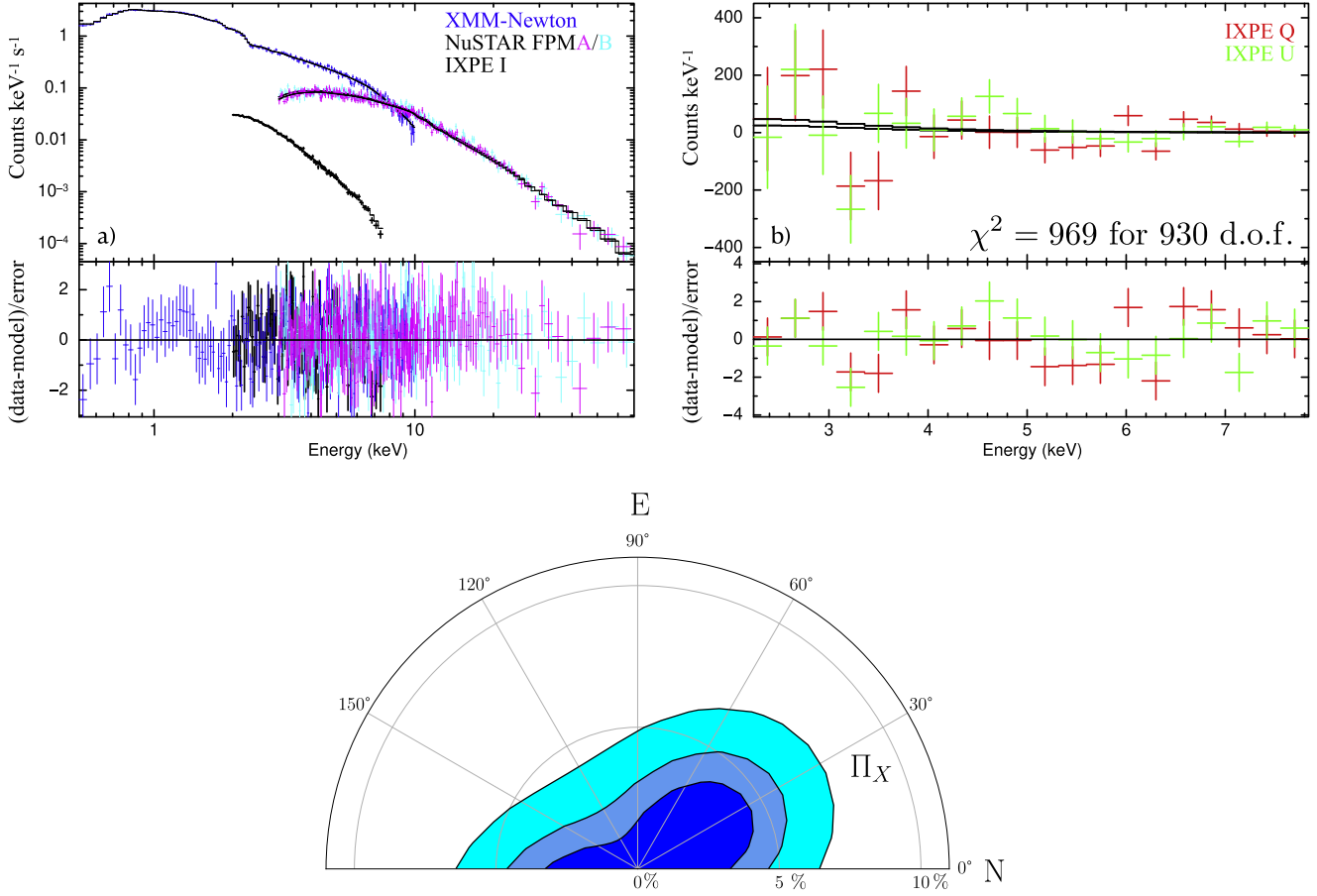


Figure 5. Top panels: best fit to the IXPE, XMM-Newton, and NuSTAR data and corresponding residuals. On the left, the model $\text{tbabs} \times \text{const} \times \text{polconst} \times \text{po}$ fitting the I Stokes spectra is shown, while the right panel displays the best-fit Q and U Stokes spectra. Bottom panel: confidence regions corresponding to 68%, 90%, and 99% uncertainties derived using the full IXPE 2–8 keV data.

Table 3
Best-fit Parameters for the Joint X-Ray Observations

Component	Parameter	Value	Units
polconst	Π_X	<7.4% (C. L. 99.73%)	...
	Ψ_X
tbabs	N_H	2.45 ± 0.07	$\times 10^{21} \text{ cm}^{-2}$
	Γ	1.87 ± 0.01	...
	Norm	6.72 ± 0.01	$\times 10^{-3} \text{ photons keV}^{-1} \text{ cm}^{-2} \text{ s}^{-1}$
const	k_{DU2}	0.97 ± 0.01	...
const	k_{DU3}	0.88 ± 0.01	...
const	k_{pn}	0.78 ± 0.01	...
const	k_{FPMA}	1.07 ± 0.02	...
const	k_{FPMB}	1.11 ± 0.02	...
$F_{2-8 \text{ keV}}$		1.75 ± 0.01	$\times 10^{-11} \text{ erg cm}^{-2} \text{ s}^{-1}$
$F_{2-10 \text{ keV}}$		1.60 ± 0.02	$\times 10^{-11} \text{ erg cm}^{-2} \text{ s}^{-1}$
$F_{0.5-2 \text{ keV}}$		6.45 ± 0.05	$\times 10^{-12} \text{ erg cm}^{-2} \text{ s}^{-1}$

Note. All uncertainties are quoted at a 68% confidence level for one parameter of interest. The 2–8 keV flux is estimated from the IXPE data, while fluxes in the 0.5–2 and 2–10 keV bands are derived from the XMM-Newton data.

NuSTAR observed BL Lac simultaneously with IXPE for a total of ~ 20 ks from 2023 November 13 16:11:09 to 2023 November 14 02:51:09. The FPMA/B instruments carried on its focal plane operate in the 3–79 keV range, thereby providing

unique broadband data. Science products of BL Lac were obtained by employing the NuSTARDAS software, also developed by the ASI-SSDC and included in the NASA-HEASARC HEAsoft package, and the latest calibration data files CALDB (version family 20220510). We used a circular region (radius $r \sim 70''$) centered on BL Lac to extract both the FPMA and FPMB spectra. The same-sized region but located on a black area of the detectors was used to extract the background. The ancillary and response matrices were computed at this stage, and we grouped the spectra via the grpahf standard command in order to have at least 30 counts bin^{-1} .

B.3. Time-averaged Spectropolarimetric Analysis

Our search for a polarized X-ray signal from BL Lac relied on a spectropolarimetric analysis in which we simultaneously modeled the IXPE, XMM-Newton, and NuSTAR spectra. We proceeded in the manner of R. Middei et al. (2023), where a similar data set was analyzed. In particular, we tested a simple phenomenological model in XSPEC that can be written as $\text{tbabs} \times \text{const} \times \text{po} \times \text{polconst}$. The first component accounts for the column density through gas in our Galaxy and whatever additional hydrogen might intercept our line of sight (e.g., T. M. Bania et al. 1991; G. M. Madejski et al. 1999; R. Middei et al. 2023). The constant is used for the intercalibration of the different telescopes, and the power law

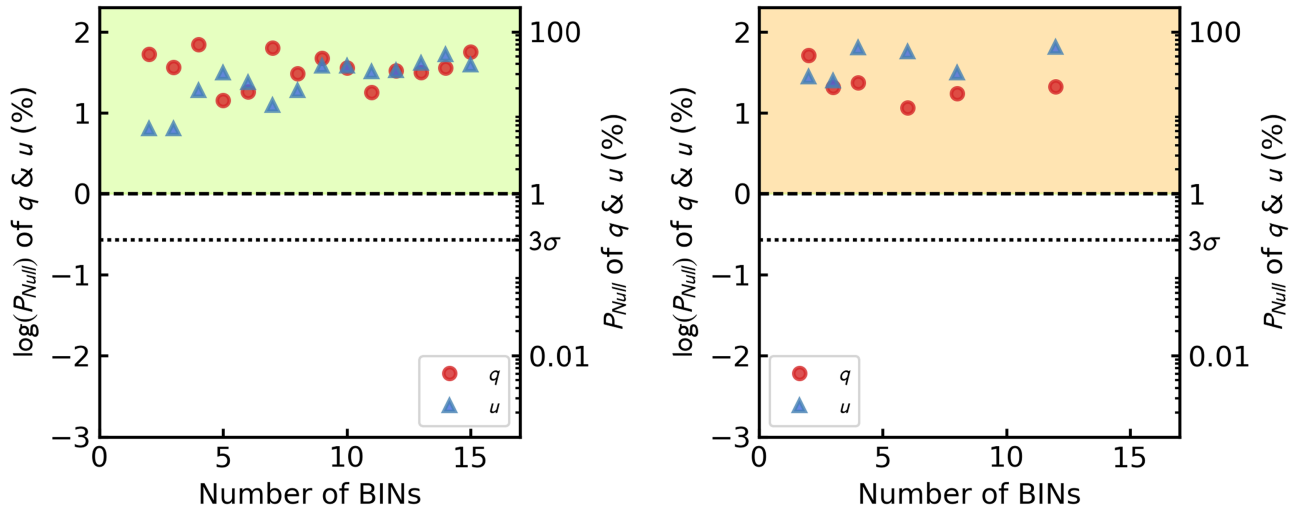


Figure 6. Null hypothesis probability of a constant model of the q (red) and u (blue) Stokes parameters for different time (left panel) and energy (right panel) bins. The green and orange shaded areas indicate that the null hypothesis probability is above the 1% threshold level. The black dashed and dotted lines located in the middle of each panel represent 1% and 3σ (0.27%) probability, respectively. The left and right vertical axes of each panel correspond to the probability values in logarithmic and linear scales in percentage, respectively.

describes the X-ray continuum spectrum. The polarization signal is encoded in the Q and U Stokes spectra and determined from the multiplicative component *polconst*, which assumes the X-ray polarized signal to be constant in the IXPE operating band.

The spectropolarimetric fit is performed by computing the photon index of the continuum and its normalization, the polarization degree Π_X and polarization angle Ψ_X , and five constants accounting for the DU1, DU2, and DU3 DUs of IXPE, the EPIC-pn camera, and the FPMA/B modules of NuSTAR. These simple steps returned a fit with $\chi^2/\text{d.o.f.} = 1039/932$. Similarly to the discussion in R. Middei et al. (2023), the observed column density exceeds the Galactic value and the EPIC-pn spectrum shows bump-like residuals around 0.7 keV that may be due to some additional spectral component. We investigated the possible origin of these bump-like residuals by examining whether the unmodeled data could be attributed to a steep upper tail of the synchrotron spectrum entering the XMM-Newton bandpass. To test this, we replaced the Gaussian line by a second power law for which the photon index and the normalization were fitted. However, this attempt returned a poorer fit with $\chi^2/\text{d.o.f.} = 638/553$. As a second test, we replaced the two power laws with a broken power law (BKNPO in XSPEC notation) and fit the two Γ the break energy and the normalization of the power law. This second attempt yielded a better fit ($\chi^2 = 556$ for 553 d.o.f.), but the very flat soft spectral shape predicted by this model ($\Gamma_{\text{soft}} \sim 0.2$) is not consistent with the hypothesis of a soft synchrotron component extending up to ~ 2 keV. We thus proceeded as in R. Middei et al. (2023) and updated our fitting model to include an unpolarized *apec* component that could explain the excess in the soft X-ray band as emission from hot diffuse plasma. The addition of this Gaussian component is beneficial in terms of χ^2 , as the statistic improved by $\Delta\chi^2/\Delta\text{d.o.f.} = -70/-2$. This best-fitting model is shown in Figure 5, and the inferred quantities are reported in Table 3. Our analysis reveals that the X-ray spectrum of BL Lac beyond ~ 2 keV was well represented by a power law with photon index $\Gamma = 1.87 \pm 0.01$. The density of the absorbing column, although exceeding the Galactic value, was found to be $N_H = 2.45 \pm 0.05 \times 10^{21} \text{ cm}^{-2}$, in agreement with previous

studies (e.g., Z. R. Weaver et al. 2020). Below the IXPE bandpass, the EPIC-pn spectrum seems compatible with emission from hot gas ($kT = 0.38 \pm 0.04$ keV), although a physical origin for such a hot gas is unknown and requires further study.

According to our analysis, no significant polarization of BL Lac was measured by IXPE during the campaign. The 3σ (99.73% confidence level) upper limit to the polarization degree is $\Pi_X^{3\sigma} < 7.4\%$, while the corresponding value at the 99% confidence level is $\Pi_X^{99} < 6.6\%$. No indications of significant polarization could be found by altering the energy range. Finally, all cross-normalization constants are in agreement with each other within $\sim 20\%$.

B.4. Time-binned IXPE Polarization Analysis

We examined polarization variability over time and energy using a χ^2 test by dividing the entire observation into specific time and energy bins, as described in D. E. Kim et al. (2024). The χ^2 analysis was performed to estimate the null hypothesis probability (P_{Null}) of a constant model fit to the time-averaged q and u values of each bin obtained from the independent spectral modeling analysis. In the case of time variability, we estimated the time-averaged q and u values by dividing the entire observation period into specific subperiods after dividing the data into 2–15 bins (e.g., 2 bins = 515 ks/2 bins = 258 ks bin $^{-1}$). To test for energy dependence, we divided the entire energy band (2–8 keV) into smaller energy bins, such as two energy bins (2–4 and 4–8 keV), three (2–4, 4–6, and 6–8 keV), and so on (up to 12). Figure 6 illustrates the calculated P_{Null} of q and u in percentage units for all of the different time binning cases. We found no statistically significant change in polarization when dividing the data into narrower time or energy ranges, with a probability higher than the 1% threshold in all cases.

We furthermore performed a study of the change in polarization over time. The data set was divided into equal intervals, and the polarimetric analysis was performed on each of them. Several interval durations were tested, and a compatible result was obtained in each case. As a trade-off, we show the division in six time bins that provide higher time resolution and reasonable statistics in each time bin. We treated

the background as in the time-averaged analysis and, as before, considered a weighted method. We used both a spectro-polarimetric analysis and the model-independent analysis described in F. Kislat et al. (2015). In the former case, we tested a simple phenomenological XSPEC model that can be written as $\text{tbabs} \times \text{constant} \times \text{pow} \times \text{polconst}$. In the latter, we applied the same method as for the time-averaged analysis. Several statistical tests were applied; the unpolarized model could not be rejected above the $\sim 3\sigma$ level in any bin or under any condition. Given the current sensitivity, no significant polarization detection can therefore be claimed. We have also performed several tests to look for the energy dependence of the polarization. For this purpose, we tested the spectral model with `pollin` in XSPEC for each time bin. No significant energy dependence of the polarization was found.

Finally, because rotation of the EVPA during the IXPE observations could affect the measurement of the polarization degree, we have also checked the data for such a rotation. Using a 1-D test for EVPA rotation (L. Di Gesu et al. 2023) we found evidence at 99.5% confidence for a rotation of $12 \pm 3.5^\circ/\text{day}$ in the 2–8 keV band. Furthermore, dividing the data into four independent intervals and allowing for EVPA rotation in each interval, i , we find that the likelihood that the polarization is zero is rejected at 99.2% confidence. This method involves computing

$$S = \sum_i^N [S_i(\hat{q}_i, \hat{u}_i, \hat{R}_i) - S_i(0, 0, 0)]$$

where $N = 4$, \hat{q}_i , \hat{u}_i , and \hat{R}_i are the best fit parameters and S_i is the event-based log-likelihood computed for the interval i (L. Di Gesu et al. 2022; H. L. Marshall 2024). Thus, S is the 3-D likelihood ratio test of the hypothesis that the polarization is zero for all intervals and is distributed as χ^2 with $3N$ degrees of freedom. Finally, assuming $R = 12^\circ/\text{day}$, the source polarization is $5.57 \pm 1.75\%$.

Appendix C Optical Data

Optical observations covering the entirety of the IXPE exposure were obtained at the Belogradchik Observatory (R band; R. Bachev et al. 2023), Calar Alto Observatory (CAFOS, R band; J. Escudero Pedrosa et al. 2024b), Nordic Optical Telescope (ALFOSC, R band; K. Nilsson et al. 2018), Liverpool Telescope (MOPTOP, BVR bands; M. Shrestha et al. 2020), LX-200 photometry ($BVRI$ bands) and polarimetry (R band), Perkins Telescope (PRISM; $BVRI$ bands, photometry, and polarimetry, S. G. Jorstad et al. 2010), Sierra Nevada Observatory (DIPOL-1, R band; J. Otero-Santos et al. 2024), and Skinakas Observatory (RoboPol, R band; A. N. Ramaprakash et al. 2019). The CAFOS and DIPOL-1 observations were analyzed using IOP4 (J. Escudero Pedrosa et al. 2024a, 2024b), while the RoboPol observations used the automatic pipeline described in G. Panopoulou et al. (2015) and D. Blinov et al. (2021). The 40 cm LX-200 telescope uses an imaging photopolarimeter with an ST-7 camera and two Savart plates oriented 45° with respect to

each other. The R -band polarization observations were corrected for interstellar and instrumental polarization using standard stars.

In the case of BL Lac, as well as many other BL Lac-type objects, the host galaxy contributes significantly to the total optical emission. This leads to dilution of the intrinsic polarization degree. To account for this effect, we use the host-galaxy light-distribution model from K. Nilsson et al. (2007) to estimate the contribution of the host galaxy to the flux density (in mJy) at the aperture used for the polarization analysis for each observatory. We then correct the observed polarization degree by subtracting the host flux density from the total flux density following T. Hovatta et al. (2016). Since we only have a model for the host galaxy in the R band, only the R -band measurements have been corrected. In this case the correction is small, yielding a change of only 1%–3%. Although we have not corrected the other optical bands, the brightness of a typical elliptical galaxy, as is the case for the host galaxy of BL Lac, falls sharply toward higher frequencies. The host correction in the B and V bands is typically negligible, while is it more significant in the I band.

The optical polarization measurements are shown in Figure 7. We see achromatic variations in brightness and polarization properties. There is a high-amplitude outburst in polarization degree that coincides with the IXPE observation. The polarization degree starts at 4%, rises to 47.5%, then declines to 16% from the beginning to the end of the IXPE observation. This matches the highest polarization ever reported from a blazar (the previous record of $47.4\% \pm 0.1\%$ was observed in PKS 1502 +106; P. S. Smith 2017). At the same time, there is a less prominent flare in optical total flux. The polarization angle slowly drifts from 70° to 30° with a median of 45° , without any indications of large variations or rotations, as are often exhibited by BL Lac (e.g., A. P. Marscher et al. 2008; D. Blinov et al. 2018). This particular optical behavior of BL Lac will be studied in detail in a forthcoming publication.

In order to provide a general overview of the behavior of BL Lac as compared to the one during this campaign, we have retrieved the historical photopolarimetric R -band data from different observatories and databases. This includes measurements from Steward Observatory⁷⁵ (2008–2018; P. S. Smith et al. 2009), Skinakas Observatory (RoboPol,⁷⁶ 2013–2017; D. Blinov et al. 2021), Calar Alto Observatory (CAFOS; I. Agudo et al. 2012), Sierra Nevada Observatories (2007–2024), Perkins Telescope (2005–2023), LX-200 and AZT-8 telescopes (2005–2023), Nordic Optical Telescope (NOT; 2015–2020), and Tuorla blazar monitoring (KVA; 2003–2011), covering a period of more than 20 yr. These data are shown in Figure 1. BL Lac is known for its remarkable variability across all bands, as exemplified by the past several bright flares, which reached optical magnitudes as bright as $R \sim 11$. Extreme flares have also been observed in X-rays and γ -rays from this source. However, as shown by the variations in polarization degree over ~ 20 yr of monitoring, the nature of the event observed during the IXPE campaign is unique, reaching an all-time maximum polarization degree for any blazar. Interestingly, this feature coincides with a very low γ -ray emission state of BL Lac, as shown by the Fermi-LAT data, and with a relatively modest optical flare.

⁷⁵ <https://james.as.arizona.edu/~psmith/Fermi/>

⁷⁶ <https://robopol.physics.uoc.gr>

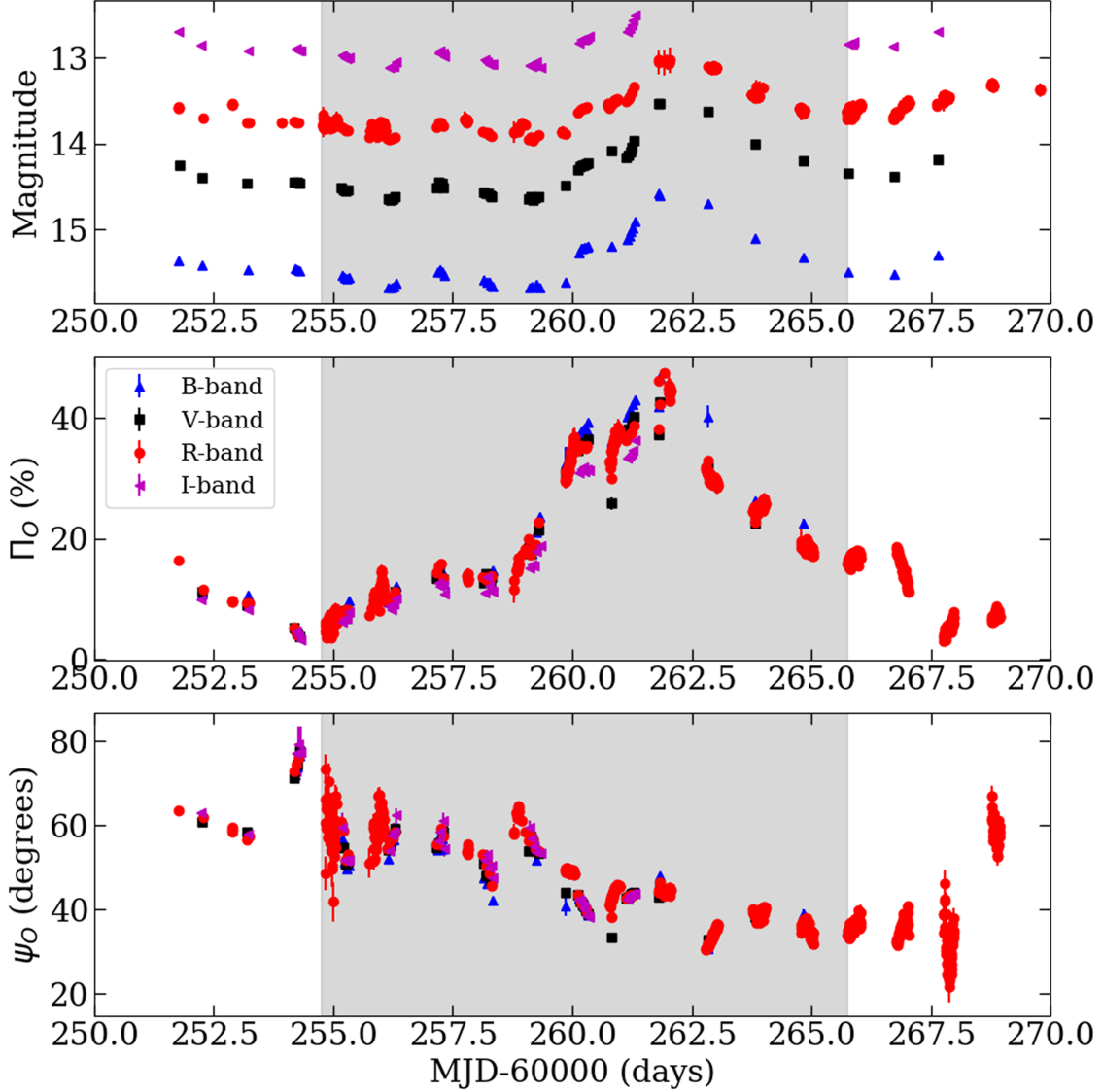


Figure 7. Optical polarization measurements during the IXPE observation. The top panel shows the brightness in magnitudes, the middle panel the polarization degree (%), and the bottom panel the polarization angle (degrees). The gray shaded area marks the duration of the IXPE observation. The different optical bands are marked with different symbols and colors as shown in the legend. The error bars correspond to the 68% (1σ) confidence interval.

Appendix D Radio/Millimeter Data

BL Lac was observed from 4 to 225.5 GHz by the Effelsberg 100 m telescope as part of the QUIVER (Monitoring the Stokes Q , U , I and V Emission of AGN jets in Radio) program (4.8, 10.4, 13.8, and 14.2 GHz; A. Kraus et al. 2003; I. Myserlis et al. 2018), by the Korean VLBI Network (KVN; 25, 43, 86, and 129 GHz; S. Kang et al. 2015), and by the Submillimeter Array (SMA) within the framework of the SMA Monitoring of AGNs with Polarization (SMAPOL) program (225.5 GHz; P. T. P. Ho et al. 2004; D. P. Marrone & R. Rao 2008; R. A. Primiani et al. 2016).

Figure 8 shows the contemporaneous radio observations. We find a similar behavior as in the optical observations. There is a brightening across frequencies that coincides with a sharp peak in the polarization degree, best visible in the better-sampled 225.5 GHz observations. As usual in blazars (e.g., I. Agudo et al. 2018a), there is an increase of the polarization degree toward higher frequencies. At low radio frequencies

(<86 GHz), the polarization degree is in the range 1%–6%. At higher frequencies (≥ 86 GHz), the polarization degree is between 6% and 10%. There is a similar trend in the polarization angle at 225.5 GHz, from 85° to 51° , as we observe in the optical bands, although the polarization angle in the radio bands is higher than the optical. The jet axis on the plane of the sky is found to be $10^\circ \pm 2^\circ$ (Z. R. Weaver et al. 2022); hence, the radio and optical polarization angles wander by tens of degrees from the jet direction. (However, see the discussion of contemporaneous VLBA images below for a different viewpoint.)

We have also extended the 1 mm radio light curve with the archival data from SMA available since 2002 (M. A. Gurwell 2007) and the Polarimetric Monitoring of AGN at Millimeter Wavelengths (POLAMI; see I. Agudo et al. 2018b) program running at the 30 m IRAM Millimeter Radio Telescope since 2010 (and at 3 mm since 2006). The historical 1 mm flux density and polarization degree light versus time are displayed in the bottom panels of Figure 1. From the 1 mm flux density

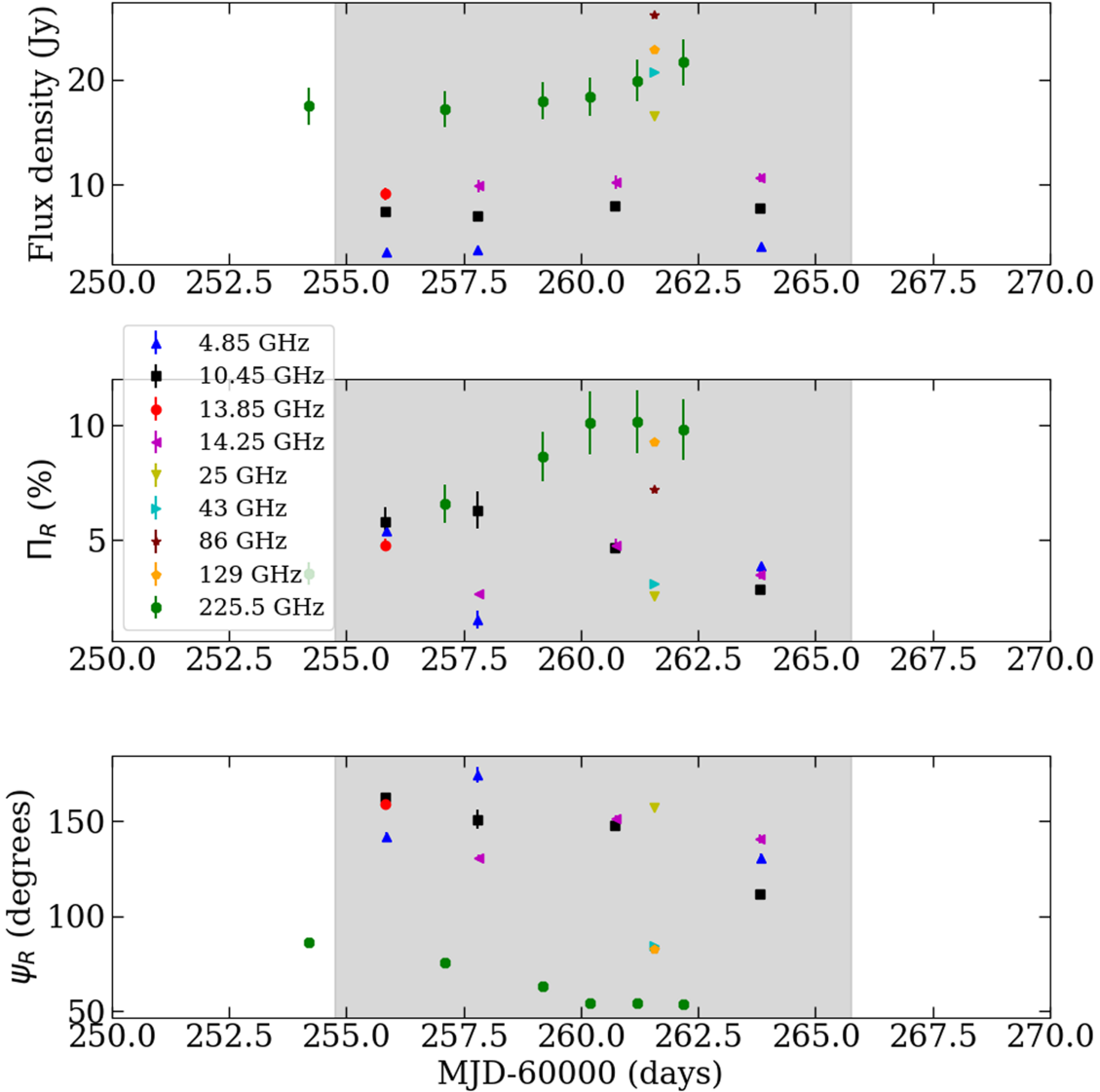


Figure 8. Short millimeter wavelength and radio polarization measurements during the IXPE observation. The top panel shows the flux density, the middle panel the polarization degree, and the bottom panel the polarization angle. The gray shaded area marks the duration of the IXPE observation. The different radio frequencies are marked with different symbols and colors as shown in the legend. The error bars correspond to the 68% (1 σ) confidence level.

evolution, it is clear that this IXPE observing window coincides with the brightest total flux ever observed from BL Lac, with the two previous highest states, corresponding to two fast flares in 2012 and 2022, being a factor of 1.5 weaker than the late 2023 level. Comparison with the archival POLAMI observations reveals that the polarization degree in the 1 mm band during this period was above the average value observed for this source.

We also analyzed a set of six ultrahigh angular resolution VLBA images from the 7 mm BEAM-ME program⁷⁷ from 2023 October 13 to 2024 February 11; see Figure 9. The data were reduced, calibrated, imaged, and model-fit as in S. G. Jorstad et al. (2017). The 7 mm VLBA images show that there is a significant change of polarization angle in the VLBI core between November 6 and 25 from -24° to $+53^\circ$. In agreement with the sharp total flux emission peak seen in the

1 mm light curve (e.g., Figure 1), these two VLBA observing epochs have the highest map peak of 15.14 and 16.24 Jy beam $^{-1}$, respectively, over all BEAM-ME observations started in 2007 June. (Note that the size of the beam is the same.) On December 12, the polarization angle in the innermost jet region is $\sim 40^\circ$, close to the optical median value. Also, the direction of this innermost jet region in 2023 November is 42° , very close to the polarization angle in the optical and in the brightest VLBI core emission at 43 GHz on November 24. This behavior is consistent with that expected from a plane-perpendicular shock wave propagating from the innermost bent jet regions in BL Lac just after the optical total flux and polarization flare reported in Figure 7. The close time coincidence of this millimeter-wave and optical behavior strongly suggests that the site of the extreme optical behavior reported in this Letter is in the VLBI core region in BL Lac.

⁷⁷ See <https://www.bu.edu/blazars/BEAM-ME.html>.

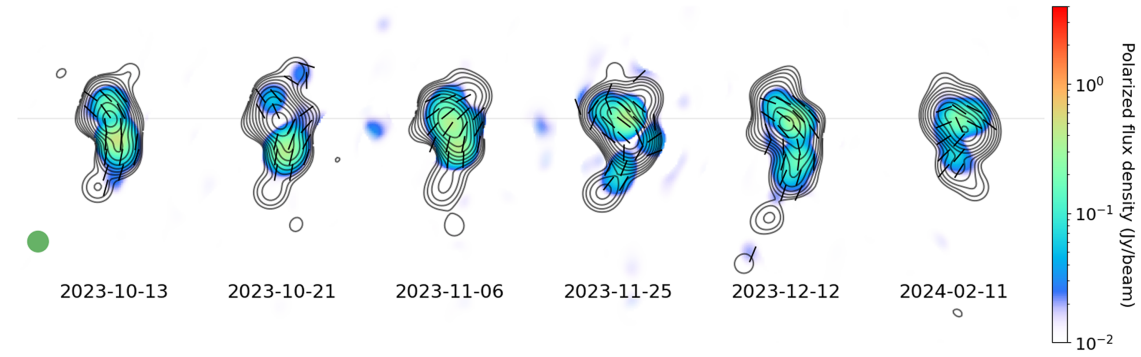


Figure 9. Sequence of 43 GHz VLBA images of BL Lac from the BEAM-ME program at 0.1 mas angular resolution. Contours represent total flux density from $0.01 \text{ Jy beam}^{-1}$ (the lowest contour on every image) to $5.50 \text{ Jy beam}^{-1}$ (the highest contour). There are 10 logarithmically equally spaced total flux contours from those minimum and maximum levels. The short sticks symbolize the direction of the electric vector polarization angle.

Appendix E Broadband Spectral Index Analysis

We have conducted an evaluation of the spectral indices of the different bands along the electromagnetic spectrum, finding further evidence for the leptonic SSC nature of the high-energy emission observed from BL Lac. For this, we have used the PYTHON package JetSet⁷⁸ (A. Tramacere et al. 2009, 2011; A. Tramacere 2020), which contains an already-implemented routine that allows calculation of the spectral (α) and photon indices (Γ , with $\Gamma = \alpha - 1$) in different frequency ranges of the electromagnetic spectrum through a power-law fit. In particular, we have calculated the spectral indices in the radio-to-millimeter (10^{10} – 10^{11} Hz), millimeter-to-IR (10^{11} – 10^{13} Hz), IR-to-optical ($10^{12.2}$ – $10^{14.8}$ Hz), optical-to-UV (10^{14} – 10^{16} Hz), X-ray

(10^{16} – 10^{19} Hz), and MeV-to-GeV ($10^{22.38}$ – $10^{25.38}$ Hz) bands. The derived spectral and photon index values are reported in Table 4. In Figure 3, we plot the flux density F_ν (in units of $\text{erg cm}^{-2} \text{s}^{-1} \text{Hz}^{-1}$) versus frequency based on the spectral fits performed in each band.

Our broadband spectral index analysis clearly indicates that the optical and γ -ray spectra have essentially the same slope, while the X-ray spectral index lies between the millimeter-to-IR and the IR-to-optical values. This is exactly the broadband spectral behavior expected for an SSC scenario, where the γ -rays are produced by Compton scattering of the optical synchrotron photons by the same electrons that emit the optical radiation, while the IR synchrotron photon field is the seed for the X-ray SSC emission, upscattered by the IR-emitting electrons.

Table 4
Results of the Spectral Analysis Performed over the Different Frequency Bands, Comparing the Photon and Spectral Indices

Band	$\log \nu_{\min} [\text{Hz}]$	$\log \nu_{\max} [\text{Hz}]$	Photon Index	Spectral Index	N
Radio–millimeter	10	11	-0.55 ± 0.01	0.45 ± 0.01	13
Millimeter–IR	11	13	-1.36 ± 0.08	-0.36 ± 0.08	7
IR–optical	12.2	14.8	-2.39 ± 0.01	-1.39 ± 0.01	4
Optical–UV	14	16	-2.82 ± 0.03	-1.82 ± 0.03	10
X-rays	16	19	-1.68 ± 0.01	-0.68 ± 0.01	23
γ -rays	22.38	25.68	-2.31 ± 0.08	-1.31 ± 0.08	6

Note. The last column shows the number of energy bins N used for each fit.

⁷⁸ <https://jetset.readthedocs.io/en/latest/>

ORCID iDs

Iván Agudo [DOI](https://orcid.org/0000-0002-3777-6182)
 Ioannis Lioudakis [DOI](https://orcid.org/0000-0001-9200-4006)
 Jorge Otero-Santos [DOI](https://orcid.org/0000-0002-4241-5875)
 Riccardo Middei [DOI](https://orcid.org/0000-0001-9815-9092)
 Alan Marscher [DOI](https://orcid.org/0000-0001-7396-3332)
 Svetlana Jorstad [DOI](https://orcid.org/0000-0001-9522-5453)
 Haocheng Zhang [DOI](https://orcid.org/0000-0001-9826-1759)
 Hui Li [DOI](https://orcid.org/0000-0003-3556-6568)
 Laura Di Gesù [DOI](https://orcid.org/0000-0002-5614-5028)
 Roger W. Romani [DOI](https://orcid.org/0000-0001-6711-3286)
 Dawoon E. Kim [DOI](https://orcid.org/0000-0001-5717-3736)
 Francesco Fenu [DOI](https://orcid.org/0000-0002-0313-8852)
 Herman L. Marshall [DOI](https://orcid.org/0000-0002-6492-1293)
 Luigi Pacciani [DOI](https://orcid.org/0000-0001-6897-5996)
 Juan Escudero Pedrosa [DOI](https://orcid.org/0000-0002-4131-655X)
 Francisco José Aceituno [DOI](https://orcid.org/0000-0001-8074-4760)
 Beatriz Agís-González [DOI](https://orcid.org/0000-0001-7702-8931)
 Giacomo Bonnoli [DOI](https://orcid.org/0000-0003-2464-9077)
 Víctor Casanova [DOI](https://orcid.org/0000-0003-2036-8999)
 Daniel Morcuende [DOI](https://orcid.org/0000-0001-9400-0922)
 Vilppu Piironen [DOI](https://orcid.org/0000-0003-0186-206X)
 Alfredo Sota [DOI](https://orcid.org/0000-0002-9404-6952)
 Pouya M. Kouch [DOI](https://orcid.org/0000-0002-9328-2750)
 Elina Lindfors [DOI](https://orcid.org/0000-0002-9155-6199)
 Callum McCall [DOI](https://orcid.org/0000-0002-3375-3397)
 Helen E. Jermak [DOI](https://orcid.org/0000-0002-1197-8501)
 Iain A. Steele [DOI](https://orcid.org/0000-0001-8397-5759)
 George A. Borman [DOI](https://orcid.org/0000-0002-7262-6710)
 Tatiana S. Grishina [DOI](https://orcid.org/0000-0002-3953-6676)
 Vladimir A. Hagen-Thorn [DOI](https://orcid.org/0000-0002-6431-8590)
 Evgenia N. Kopatskaya [DOI](https://orcid.org/0000-0001-9518-337X)
 Elena G. Larionova [DOI](https://orcid.org/0000-0002-2471-6500)
 Daria A. Morozova [DOI](https://orcid.org/0000-0002-9407-7804)
 Sergey S. Savchenko [DOI](https://orcid.org/0000-0003-4147-3851)
 Ekaterina V. Shishkina [DOI](https://orcid.org/0009-0002-2440-2947)
 Ivan S. Troitskiy [DOI](https://orcid.org/0000-0002-4218-0148)
 Yulia V. Troitskaya [DOI](https://orcid.org/0000-0002-9907-9876)
 Andrey A. Vasilyev [DOI](https://orcid.org/0000-0002-8293-0214)
 Ioannis Myserlis [DOI](https://orcid.org/0000-0003-3025-9497)
 Mark Gurwell [DOI](https://orcid.org/0000-0003-0685-3621)
 Garrett Keating [DOI](https://orcid.org/0000-0002-3490-146X)
 Ramprasad Rao [DOI](https://orcid.org/0000-0002-1407-7944)
 Sincheol Kang [DOI](https://orcid.org/0000-0002-0112-4836)
 Sang-Sung Lee [DOI](https://orcid.org/0000-0002-6269-594X)
 Sanghyun Kim [DOI](https://orcid.org/0000-0001-7556-8504)
 Whee Yeon Cheong [DOI](https://orcid.org/0009-0002-1871-5824)
 Hyeon-Woo Jeong [DOI](https://orcid.org/0009-0005-7629-8450)
 Emmanouil Angelakis [DOI](https://orcid.org/0000-0001-7327-5441)
 Alexander Kraus [DOI](https://orcid.org/0000-0002-4184-9372)
 Dmitry Blinov [DOI](https://orcid.org/0000-0003-0611-5784)
 Siddharth Maharana [DOI](https://orcid.org/0000-0002-7072-3904)
 Jenni Jormanainen [DOI](https://orcid.org/0000-0003-4519-7751)

Kari Nilsson [DOI](https://orcid.org/0000-0002-1445-8683)
 Vandan Fallah Ramazani [DOI](https://orcid.org/0000-0001-8991-7744)
 Carolina Casadio [DOI](https://orcid.org/0000-0003-1117-2863)
 Antonio Fuentes [DOI](https://orcid.org/0000-0002-8773-4933)
 Efthalia Traianou [DOI](https://orcid.org/0000-0002-1209-6500)
 Clemens Thum [DOI](https://orcid.org/0009-0006-5292-6974)
 Lucio Angelo Antonelli [DOI](https://orcid.org/0000-0002-5037-9034)
 Matteo Bachetti [DOI](https://orcid.org/0000-0002-4576-9337)
 Luca Baldini [DOI](https://orcid.org/0000-0002-9785-7726)
 Wayne H. Baumgartner [DOI](https://orcid.org/0000-0002-5106-0463)
 Ronaldo Bellazzini [DOI](https://orcid.org/0000-0002-2469-7063)
 Stefano Bianchi [DOI](https://orcid.org/0000-0002-4622-4240)
 Stephen D. Bongiorno [DOI](https://orcid.org/0000-0002-0901-2097)
 Raffaella Bonino [DOI](https://orcid.org/0000-0002-4264-1215)
 Alessandro Brez [DOI](https://orcid.org/0000-0002-9460-1821)
 Niccolò Bucciantini [DOI](https://orcid.org/0000-0002-8848-1392)
 Fiamma Capitanio [DOI](https://orcid.org/0000-0002-6384-3027)
 Simone Castellano [DOI](https://orcid.org/0000-0003-1111-4292)
 Elisabetta Cavazzuti [DOI](https://orcid.org/0000-0001-7150-9638)
 Chien-Ting Chen [DOI](https://orcid.org/0000-0002-4945-5079)
 Stefano Ciprini [DOI](https://orcid.org/0000-0002-0712-2479)
 Enrico Costa [DOI](https://orcid.org/0000-0003-4925-8523)
 Alessandra De Rosa [DOI](https://orcid.org/0000-0001-5668-6863)
 Ettore Del Monte [DOI](https://orcid.org/0000-0002-3013-6334)
 Niccolò Di Lalla [DOI](https://orcid.org/0000-0002-7574-1298)
 Alessandro Di Marco [DOI](https://orcid.org/0000-0003-0331-3259)
 Immacolata Donnarumma [DOI](https://orcid.org/0000-0002-4700-4549)
 Victor Doroshenko [DOI](https://orcid.org/0000-0001-8162-1105)
 Michal Dovčiak [DOI](https://orcid.org/0000-0003-0079-1239)
 Steven R. Ehlert [DOI](https://orcid.org/0000-0003-4420-2838)
 Teruaki Enoto [DOI](https://orcid.org/0000-0003-1244-3100)
 Yuri Evangelista [DOI](https://orcid.org/0000-0001-6096-6710)
 Sergio Fabiani [DOI](https://orcid.org/0000-0003-1533-0283)
 Riccardo Ferrazzoli [DOI](https://orcid.org/0000-0003-1074-8605)
 Javier A. García [DOI](https://orcid.org/0000-0003-3828-2448)
 Shuichi Gunji [DOI](https://orcid.org/0000-0002-5881-2445)
 Jeremy Heyl [DOI](https://orcid.org/0000-0001-9739-367X)
 Wataru Iwakiri [DOI](https://orcid.org/0000-0002-0207-9010)
 Philip Kaaret [DOI](https://orcid.org/0000-0002-3638-0637)
 Vladimir Karas [DOI](https://orcid.org/0000-0002-5760-0459)
 Fabian Kislat [DOI](https://orcid.org/0000-0001-7477-0380)
 Jeffery J. Kolodziejczak [DOI](https://orcid.org/0000-0002-0110-6136)
 Henric Krawczynski [DOI](https://orcid.org/0000-0002-1084-6507)
 Fabio La Monaca [DOI](https://orcid.org/0000-0001-8916-4156)
 Luca Latronico [DOI](https://orcid.org/0000-0002-0984-1856)
 Simone Maldera [DOI](https://orcid.org/0000-0002-0698-4421)
 Alberto Manfreda [DOI](https://orcid.org/0000-0002-0998-4953)
 Frédéric Marin [DOI](https://orcid.org/0000-0003-4952-0835)
 Andrea Marinucci [DOI](https://orcid.org/0000-0002-2055-4946)
 Francesco Massaro [DOI](https://orcid.org/0000-0002-1704-9850)
 Giorgio Matt [DOI](https://orcid.org/0000-0002-2152-0916)

- Primiani, R. A., Young, K. H., Young, A., et al. 2016, *JAI*, **5**, 1641006
 Ramaprakash, A. N., Rajarshi, C. V., Das, H. K., et al. 2019, *MNRAS*, **485**, 2355
 Ripperda, B., Liska, M., Chatterjee, K., et al. 2022, *ApJL*, **924**, L32
 Roming, P. W. A., Kennedy, T. E., Mason, K. O., et al. 2005, *SSRv*, **120**, 95
 Shepherd, M. C. 1997, in ASP Conf. Ser. 125, Astronomical Data Analysis Software and Systems VI, ed. G. Hunt & H. Payne (San Francisco, CA: ASP), 77
 Shrestha, M., Steele, I. A., Piascik, A. S., et al. 2020, *MNRAS*, **494**, 4676
 Smith, P. S. 2017, *ATel*, **11047**, 1
 Smith, P. S., Montiel, E., Rightley, S., et al. 2009, arXiv:0912.3621
 Strüder, L., Briel, U., Dennerl, K., et al. 2001, *A&A*, **365**, L18
 Telescope Array Collaboration, Abbasi, R. U., Allen, M. G., et al. 2023, *Sci*, **382**, 903
 Tramacere, A., 2020 JetSeT: Numerical Modeling And SED Fitting Tool For Relativistic Jets, Astrophysics Source Code Library, ascl:2009.001
 Tramacere, A., Giommi, P., Perri, M., Verrecchia, F., & Tosti, G. 2009, *A&A*, **501**, 879
 Tramacere, A., Massaro, E., & Taylor, A. M. 2011, *ApJ*, **739**, 66
 Weaver, Z. R., Jorstad, S. G., Marscher, A. P., et al. 2022, *ApJS*, **260**, 12
 Weaver, Z. R., Williamson, K. E., Jorstad, S. G., et al. 2020, *ApJ*, **900**, 137
 Weisskopf, M. C., Soffitta, P., Baldini, L., et al. 2022, *JATIS*, **8**, 026002
 Yang, H., Yuan, F., Li, H., et al. 2024, *SciA*, **10**, eadn3544
 Zhang, H., & Böttcher, M. 2013, *ApJ*, **774**, 18
 Zhang, H., Böttcher, M., & Liodakis, I. 2024, *ApJ*, **967**, 93
 Zhang, H., Deng, W., Li, H., & Böttcher, M. 2016, *ApJ*, **817**, 63
 Zhang, H., Fang, K., Li, H., et al. 2019, *ApJ*, **876**, 109
 Zhang, H., Li, H., Guo, F., & Taylor, G. 2017, *ApJ*, **835**, 125